Using excitation-energy dependent fission yields to identify key fissioning nuclei in r-process nucleosynthesis

N. Vassh,[1] R. Vogt,[2,3] R. Surman,[1] J. Randrup,[4] T. M. Sprouse,[1] M. R. Mumpower,[5]
P. Jaffke,[5] D. Shaw,[1] E. M. Holmbeck,[1] Y. Zhu,[6] and G. C. McLaughlin[6]

[1] *Department of Physics, University of Notre Dame, Notre Dame, Indiana 46556, USA*
[2] *Nuclear and Chemical Science Division, Lawrence Livermore National Laboratory, Livermore, CA 94551, USA*
[3] *Department of Physics, University of California, Davis, CA 95616, USA*
[4] *Nuclear Science Division, Lawrence Berkeley National Laboratory, Berkeley, CA 94720, USA*
[5] *Theoretical Division, Los Alamos National Laboratory, Los Alamos, NM, 87545, USA*
[6] *Department of Physics, North Carolina State University, Raleigh, North Carolina 27695 USA*
(Dated: October 19, 2018)

The possibility that nucleosynthesis in neutron star mergers may reach fissioning nuclei introduces significant uncertainties in predicting the relative abundances of r-process material from such events. We evaluate the impact of using sets of fission yields given by the GEF code for spontaneous (sf), neutron-induced ((n,f)), and β-delayed (βdf) fission processes which take into account the approximate initial excitation energy of the fissioning compound nucleus. We further explore energy-dependent fission dynamics in the r process by considering the sensitivity of our results to the treatment of the energy sharing and de-excitation of the fission fragments using the FREYA code. We show that the asymmetric-to-symmetric yield trends predicted by GEF can reproduce the high-mass edge of the second r-process peak seen in solar data and examine the sensitivity of this result to the mass model and astrophysical conditions applied. We consider the effect of fission yields and barrier heights on the nuclear heating rates used to predict kilonova light curves. We find that fission barriers influence the contribution of ^{254}Cf spontaneous fission to the heating at ~ 100 days, such that a light curve observation consistent with such late-time heating would both confirm that actinides were produced in the event and imply the fission barriers are relatively high along the ^{254}Cf β-feeding path. We lastly determine the key nuclei responsible for setting the r-process abundance pattern by averaging over thirty trajectories from a 1.2–1.4 $M_\odot$ neutron star merger simulation. We show it is largely the odd-N nuclei undergoing (Z,N)(n,f) and $(Z,N)\beta$df that control the relative abundances near the second peak. We find the "hot spots" for β-delayed and neutron-induced fission given all mass models considered and show most of these nuclei lie between the predicted $N = 184$ shell closure and the location of currently available experimental decay data.

I. INTRODUCTION

Over 60 years ago, Burbidge *et al.* suggested that nuclear fission was responsible for the behavior of supernova light curves [1]. We now know the process that synthesizes fissioning nuclei—rapid neutron capture, or r-process, nucleosynthesis—is unrelated to supernova light curves and unlikely to occur robustly, if at all, in ordinary supernovae [2, 3]. The most attractive astrophysical site for an r process that reaches fissioning nuclei is within a neutron star merger [4–10]. The electromagnetic counterpart to the GW170817 neutron star merger [11–13] indicated some thousandths of a solar mass of lanthanides were produced in the event, possibly enough for mergers to account for all of the r-process lanthanides in the galaxy if the event was typical [14]. If neutron star mergers are indeed the source of all r-process elements, including the actinides, we can look to such events as opportunities to probe fission properties.

Fission processes can play an important role in determining r-process observables such as abundance patterns and light curves. For example, lanthanide abundances can be influenced by late-time deposition of fission products, e.g. [14], and neutrons from fission can affect the amount of late-time neutron capture that sets the overall abundance pattern, e.g. [15]. Nuclear heating by fission can shape kilonova light curves [16], with the late-time heating possibly dominated by the spontaneous fission of ^{254}Cf [17]. Understanding these effects requires knowledge of fission properties for hundreds of nuclei on the neutron-rich side of stability, about which little is experimentally known. Calculations of the r process instead rely almost entirely on theoretical descriptions that vary widely. Here we examine the influence of two key fission inputs in r-process calculations: the fission fragment distributions and fission barrier heights (i.e. the maximum energy along the optimum path toward scission).

The importance of the fission fragment treatment in r-process calculations is well established [15, 18–22]. Parameterized, semi-empirical formulae based on systematics, such as those in Refs. [20, 21, 23], are an improvement over symmetric splits which assume the nucleus to divide in half, but are still a simplification of complex fission dynamics. Phenomenological descriptions, such as ABLA [24, 25] and GEF [26], take into account the influence of shell structure, fission barriers, angular momentum, and neutron emission from the excited fragments. These fission yield descriptions have also been applied in r-process simulations [19, 27, 28].

An aspect of the phenomenological descriptions of fission that has so far remained relatively unexplored in the

r process is the dependence of the yields on the excitation energy of the compound nuclei. This effect is generally assumed to be small, as the r-process temperatures are low (~ 0.1 MeV), and is often ignored. The possibility for the yields of r-process nuclei to explicitly depend on the excitation energy was considered in Ref. [29], but yield distributions were found to vary smoothly with initial energy, thus the yields at vanishing neutron bombarding energy were taken to be appropriate at all energies relevant for the r process. Here we revisit an examination of the role of excitation energy on the fission yields of r-process nuclei by treating the three main processes occurring in a fission cycling r process, namely neutron-induced, β-delayed, and spontaneous fission, with distinct initial excitation energies when determining the fission yields to apply to each process. To examine the impact of such an energy dependence on the r process, we use fission yields from the publicly available GEF code (version GEF-2016-V1-2 [30]).

We explore the sensitivity the r process to the assumptions made for the evolution of excited fission fragments by comparing results with GEF and results given an alternate treatment for the energy sharing and de-excitation. To do so we modified the published FREYA code [31, 32] to use the GEF fission fragment yields (pre prompt neutron emission) as a function of post-scission fission fragment mass, charge and total kinetic energy, as input. The fission product yields (post prompt neutron emission) and average neutron multiplicities from the two codes are compared. We explore the effect of the additional neutron emission predicted by FREYA in the r process for merger dynamical ejecta conditions.

Perhaps the most important characteristic of a heavy nucleus for predicting fission properties within a given model is the height of the fission barrier. It is well known that the fission barriers assumed for heavy, neutron-rich nuclei can have a great influence on the outcome of r-process calculations [15, 19, 23, 33, 34]. Fission barriers often determine whether the nuclear flow ($\lambda_i Y_i$ where λ_i is the rate of the reaction or decay and Y_i is the abundance) will permit the population of nuclei of interest, such as the predicted superheavy island of stability [19, 33, 35–37]. The influence of fission barriers can also lead to dramatically different conclusions regarding the origin of the second r-process peak as discussed in Ref. [23], where high fission barriers near $N = 184$ coupled with very broad fission fragment distributions caused a disappearance of this main r-process feature in neutron star merger conditions.

Here we examine results using the Finite Range Droplet Model (FRDM2012) [38], Thomas-Fermi (TF) [39], Hartree-Fock-Bogoliubov (HFB-17) [40], and Extended Thomas-Fermi with Strutinsky Integral (ETFSI) [41, 42] model masses and corresponding barriers along with the GEF+FREYA yields described above. We explore how the different termination points for the r process predicted by these models influence the final abundance pattern, and identify fissioning nuclei most ac-

cessed under a range of neutron star merger conditions. We also consider the population of ^{254}Cf and find it to be sensitive to the fission barrier treatment, as suggested recently in Ref. [43].

The paper is organized as follows: our application of GEF and implementation of FREYA is described in Section II. In Section III we explore the r-process impact of the fission yields and neutron multiplicities that result from this approach. Variations of fission barrier heights and other nuclear physics inputs are considered in Section IV. In Section V we conclude by identifying the key fissioning nuclei important in a variety of neutron star merger conditions and common to all fission barrier models considered, some of which we find to be potentially within reach of future experimental facilities.

II. GEF AND FREYA FISSION TREATMENTS

We describe the GEF and FREYA fission models, the differences between them, and how those differences affect the resulting fission product yields and average neutron multiplicities for nuclei relevant for the r process. Both codes use Monte Carlo techniques to produce fission events that provide complete kinematic information, including angular momentum, for all fission fragments. (We note that two versions of GEF are available, the stand-alone Monte Carlo version used here and a deterministic subroutine for use in codes like TALYS [44, 45].) See Refs. [26, 31] for more details. While other codes such as FIFRELIN [46] and CGMF [47] are also available, GEF and FREYA are the fastest and thus most suitable for studies that require calculations for hundreds of nuclei as is the case in this work. Here we first describe the fission fragment yields, as well as their excitation energy dependence, followed by a discussion of particle emission in GEF and FREYA and how the two models can lead to different average neutron multiplicities, relevant for these studies. All the calculations in this section, for both GEF and FREYA, are based on one million fission events generated for each fissioning isotope.

While GEF and FREYA can achieve similar end results as far as the output of complete fission events, the general approaches are rather different and worth some discussion. Like FIFRELIN and CGMF, the published version of FREYA is generally more limited in the number of isotopes available because of their approach. All three codes require the fission fragment yields and total kinetic energies (TKE) of the fragments in some form as inputs. While these codes differ in detail, the basic numerical approaches are similar. The yields are sampled to choose one of the fragments with the partner chosen to conserve mass number A and charge Z, followed by sampling of the TKE for the event. Given the masses and TKE, the total excitation energy (TXE) is obtained and shared between the two fragments according to a model-dependent prescription. Once this excitation energy sharing is complete, neutron evaporation follows.

The excitation energy dependence of the input yields is modeled based on limited energy-dependent data. Some progress has recently been made using models based on potential energy surfaces calculated in the macroscopic-microscopic approach [48, 49]. Other yields calculated from many-body approaches based on density functional theory may become available in the future but these are so far quite limited [50].

The philosophy of the GEF code is quite different, allowing a broader range of isotopes to be studied and extrapolations made to regions of the nuclear chart where no data exist. Thus GEF requires no input data for the yields and total kinetic energies, unlike all other available complete event fission codes. In addition, the calculation of the yields includes an energy dependence so that the yields are also available for a range of excitation energies. The fission fragment yields in GEF depend on three things: the fission barriers, the fission channels, and the excitation energy sharing. We will touch upon all three here.

GEF employs the Thomas-Fermi (TF) macroscopic fission barriers [51] and nuclear masses [39], along with a microscopic correction to the ground state mass and a pairing correction to the binding energy at the barrier. Additionally, GEF makes use of experimentally inferred fission barriers to derive further parameterized corrections to the TF barrier heights (see [26]). The mass and charge systematics determined from these nuclear inputs are then extrapolated to unmeasured regions.

There are four fission modes used in GEF to describe the fission fragment mass yields immediately after scission (called pre-neutron in GEF). Three of these were introduced by Brosa et al. [52]: standard 1 (S1, related to near-spherical nuclei near the doubly-magic closed proton and neutron shells at $Z = 50$ and $N = 82$), standard 2 (S2, associated with the deformed neutron shell closure at $N = 88$), and super long (SL, a symmetric mode). The fourth is a super asymmetric mode (SA or S3) introduced by Mulgin et al. [53]. These modes in GEF are determined by quantum oscillator potentials related to the macroscopic potential and the proton and neutron shells in both fragments. The locations of these shells are assumed to be the same for all fissioning systems. As implied above, the shells also affect the fragment shapes and thus their deformations. The superposition of the modes (S1, S2, SL and SA) associated with the shells as well as their interactions with the macroscopic potential determines the fragment mass distributions. Each of the four modes requires three parameters to describe each oscillator. The oscillator parameters are extracted from yields where data are available. The proximity to a closed neutron or proton shell determines whether the yields are symmetric or antisymmetric and also governs the widths of the yields in A and Z. The effects of nuclear deformation, fragment angular momentum and charge polarization on the quantum oscillator potentials are taken into account. Empirical A and Z systematics of the oscillator parameters are used to determine the yields where no data are available.

Finally, the energy sharing mechanism in GEF determines how the intrinsic (statistical) excitation energy is divided between the heavy and light fragment. Before scission, the fragments are coupled so that nucleons unpaired before scission are preferentially transferred to the heavy fragment. Again, A and Z systematics are determined from data and used to fix the fragment excitation energies at scission for unmeasured isotopes. Because the excitation energy is modeled at scission, no input TKE is required, unlike FREYA. The TKE is thus determined by energy conservation in GEF, contrary to the other fission models.

To be able to use GEF to obtain the fission fragment yields for r-process nuclei, we extended the "range of validity", defined by $A/Z < 172/80$ and $A/Z > 250/90$ for $76 < Z < 120$, implemented in the default GEF code. We do not, however, go beyond the nuclei included in the default mass and shell correction tables in the range $1 \leq Z \leq 136$ and $1 \leq N \leq 203$ to ensure that our output fission data is as consistent with standard user outputs as possible. We will later show that given astrophysical conditions leading to fission, there is minimal r-process fission flow beyond $N = 203$ for most of the nuclear mass models considered. Therefore, implementing yields for nuclei with $N \leq 203$ was deemed sufficient.

The excitation energy dependence of the GEF yields arises from two sources: the oscillator model of the fission modes and the energy sorting mechanism. We note that, at higher excitation energies, the transfer of unpaired nucleons to the heavy fragment gives the additional neutron multiplicity to the heavy fragment while the light fragment neutron multiplicity remains relatively constant. The charge polarization, determining the charge yields, is assumed to remain essentially unchanged by an increase in excitation energy. We note that, at sufficiently high excitation energies, both GEF and FREYA include multi-chance fission and pre-equilibrium neutron emission. GEF also allows the possibility of "scission neutrons" emitted between saddle and scission while FREYA does not.

Experimentally, the measured fission product yields (termed post-neutron emission in GEF) depend on the excitation energy of the compound nucleus (given by the A of the nucleus for spontaneous and beta-delayed fission and $A+1$ for neutron-induced fission). Prior evaluations of the cumulative fission yields (after both prompt and delayed emission) for three energy groups: thermal, fast (incident neutrons of several MeV) and high energy (14 MeV incident neutrons) indicate that the yields become more symmetric with increasing incident neutron energy [54]. However, a more recent experiment employing a mono-energetic neutron beam on ^{235}U, ^{238}U and ^{239}Pu targets with finer incident neutron energy bins (0.56, 1.37, 2.37, 3.60, 4.49, 5.5 and 14.8 MeV) [55] suggested a more complex dependence on the incident energy. At neutron energies $\lesssim 3 - 4$ MeV, the cumulative fission yields for ^{239}Pu(n,f) in particular show a non-monotonic
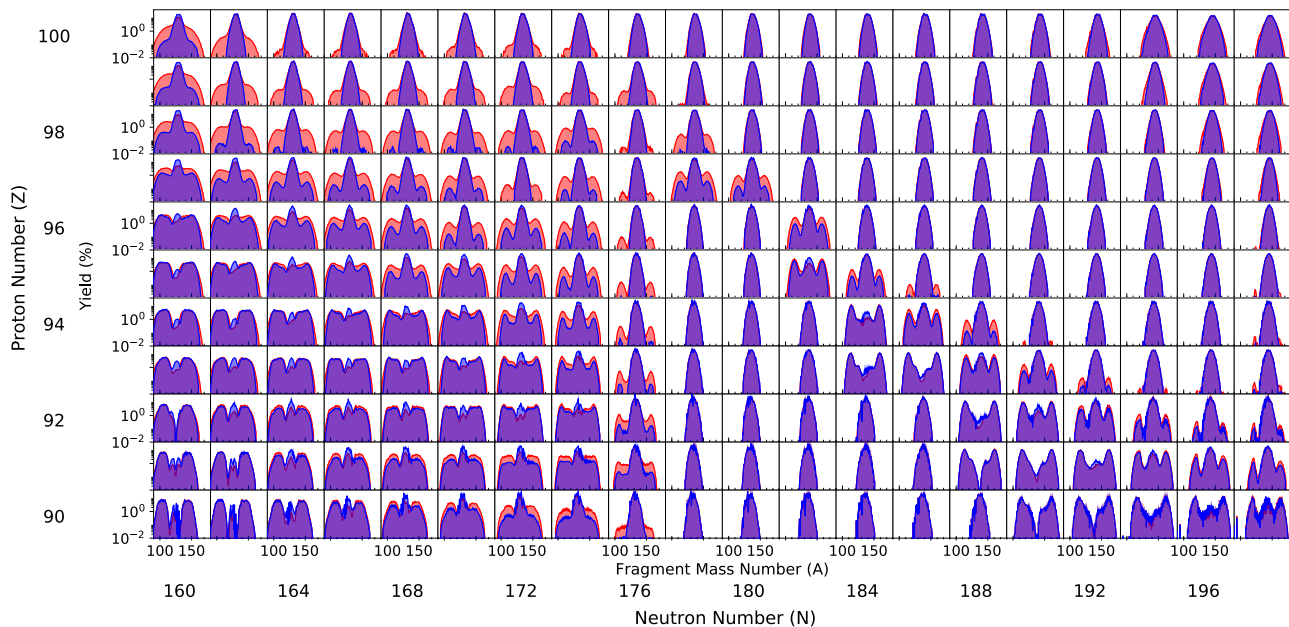
FIG. 1. (Color online) The GEF product yields from neutron-induced fission for 0.1 MeV neutrons (red) are compared to the product yields from spontaneous fission of the same compound nucleus (blue).

energy dependence for some high yield fission products (note that only 14 fission product isotopes were included in the study since gamma-ray counting was employed to measure the fission products). Thus the energy dependence of the fission yields may be more complicated than previously assumed.

Neutron-induced fission in the r process occurs late in time at low temperatures, equivalent to an incident neutron energy of ~ 0.1 MeV, lower than any of the energies employed in Ref. [55]. Nonetheless, the excitation energy for this r-process reaction, 0.1 MeV $+ S_\mathrm{n}$, is still considerably higher than the zero excitation energy of spontaneous fission and one could expect a difference in the spontaneous and neutron-induced fission yields. The resultant fission product yields are shown in Fig. 1. Some increased asymmetry is seen in the tails of the yield distributions. This behavior is reasonable since higher excitation energies generally increase the likelihood of more asymmetric splits while initially having only a small effect on the yields at symmetry.

For the neutron-rich nuclei of interest here, the GEF systematics suggest a global trend of transition from asymmetric toward symmetric yields along most isotopic chains, with a region of primarily symmetric yields near the shell closure at $N = 184$. Along an isotonic chain in this neutron-rich region, on average the yields become increasingly symmetric with increasing Z. We will later examine the impact that such asymmetric-to-symmetric yield trends have on the r-process abundance pattern and will show that the enhanced asymmetric yield contributions for finite excitation energies appear in key regions

for a fission cycling r process.

We now turn to neutron emission from the fragments and the resulting fission product yields. First we discuss how we modify FREYA to make use of the GEF fission fragment yields. We then discuss how neutron emission differs in the two codes and how, even though we may start with identical yields in both GEF and FREYA, we may end up with different fission product yields and average neutron multiplicities $\bar\nu$. The difference in neutron emission is important for the r process because the prompt fission neutron multiplicity can be a substantial fraction of the late-time neutrons available for capture in the r process [19], thereby influencing the movement of lighter nuclei near the second and third r-process abundance peaks.

The current published version of FREYA, FREYA 2.0.2 [32], as previously discussed, is limited to certain isotopes: spontaneous fission of ^{244}Cm, ^{252}Cf, ^{238}U and ^{238,240,242}Pu as well as neutron-induced fission of ^{233,235,238}U and ^{239,241}Pu. For FREYA to be used in calculating the fission yields and neutron emission relevant to the r process, it needed to be modified to incorporate the necessary inputs where no data are available. To do this, FREYA was changed to be able to use the fission fragment yields as function of mass and charge, $Y(A,Z)$, as well as the yields as a function of mass and TKE, $Y(A)$ and $Y(\mathrm{TKE})$, given by GEF. Thus, in the calculations that follow, the primary fragment yields employed in the two codes are identical and the differences are due to how neutron evaporation is treated.
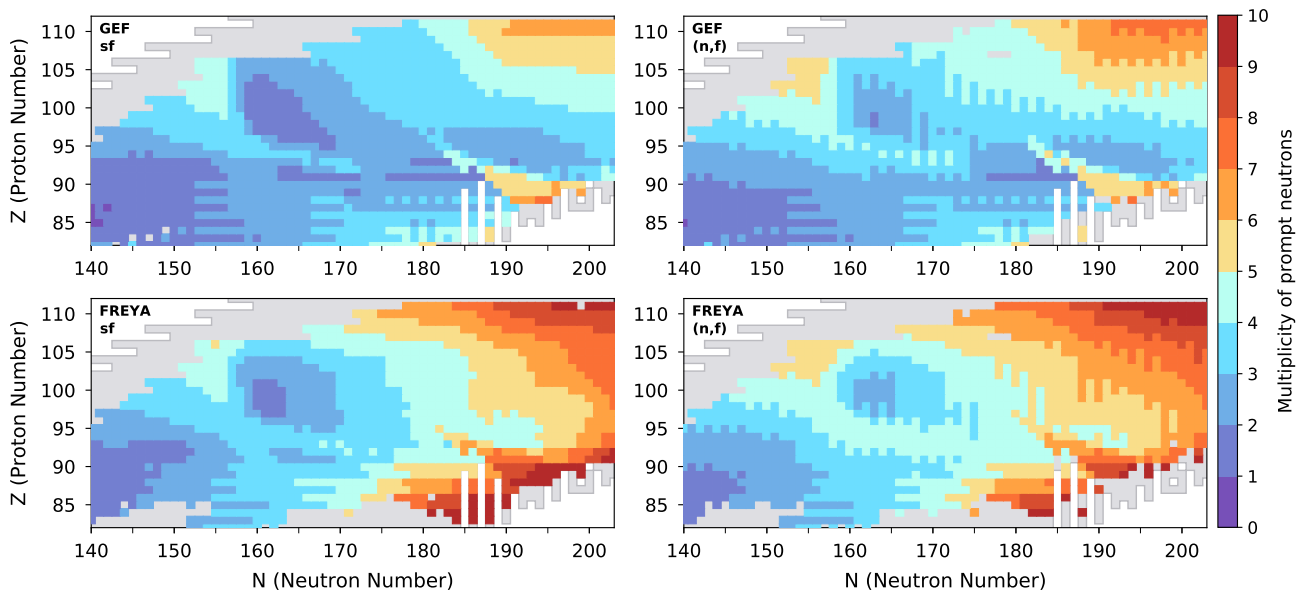
Because GEF models the excitation energy partition

FIG. 2. (Color online) The average prompt neutron multiplicity for fission induced by the capture of a 0.1 MeV neutron (right panels) compared to the multiplicity from spontaneous fission (left panels) using the energy sharing and de-excitation treatments of GEF (top panels) and FREYA (bottom panels). The grey region shows the TF dripline.

between the fragments at scission, the energy available for neutron emission is set with no additional parameters required. Neutron emission from the fully accelerated fragments in GEF proceeds through a statistical model, using the relative neutron emission width from [56]. The width depends on fragment mass, excitation energy, angular momentum, fragment temperature, and neutron separation energy. On the other hand, FREYA, like CGMF and FIFRELIN, starts with the TKE as input instead of the total excitation energy. Thus the excitation energy partition between the fragments in these codes is done empirically. FREYA 2.0.2 has five physics-based parameters: dTKE, which shifts TKE as a function of heavy fragment mass by some amount to ensure agreement with the average neutron multiplicity; x, representing additional excitation energy given to the light fragment, $x > 1$; c, setting the level of thermal fluctuations in the fragments; e_0, the value of the asymptotic level density parameter and c_S, governing the fragment spin magnitude, see Ref. [57]. We note that while the FREYA parameters can be set on a case-by-case basis, x, c_S and e_0 were shown to be effectively independent of isotope for the isotopes in FREYA that undergo spontaneous fission [58].

Because FREYA does not have any systematic way of setting the parameters for unknown isotopes, we adjust dTKE in FREYA to match the known $\bar{\nu}$ in two specific cases, ^{252}Cf(sf) and ^{239}Pu(n,f), while leaving the other parameters fixed at their default values for these isotopes. In these two cases, it was found that the dTKE required in FREYA when using the GEF yields was negligibly small. We use the ^{252}Cf(sf) parameters for all

spontaneous fission and the ^{239}Pu(n,f) parameters for all neutron-induced and beta-delayed fissions. It is clear that we will not obtain the same neutron multiplicity from FREYA and GEF since we neither employ the same methods of fragment de-excitation nor are the FREYA parameters tuned to each isotope. Indeed, there are no data for us to test the parameter values in either model. However, we can take any differences between the models as an indication of the fission uncertainties affecting the r process.

Figure 2 shows the resulting neutron multiplicities for spontaneous (left panels) and neutron-induced (right panels) fission from GEF (top panels) and FREYA (bottom panels). In both cases the multiplicities are generally higher for neutron-induced fission, with $1-2$ more neutrons emitted than for spontaneous fission. In the very neutron-rich region, the neutron multiplicities can be quite high, with $8-10$ neutrons emitted in some cases, presumably because the outer neutrons are not strongly bound and thus emission is more probable. It is also clear that more neutrons are emitted through the de-excitation process in FREYA than in GEF, even starting from the same initial fission fragment yields. We now describe where the differences in multiplicity may come from and discuss possible consequences of this difference later.

The model of excitation energy sharing in GEF is replaced in FREYA by the constant parameter x. We note that in FIFRELIN and CGMF, the excitation energy sharing is also parameterized but, in those cases, mass dependent ratios are derived from data on the measured neutron multiplicity for specific isotopes as a function of fragment mass, $\bar{\nu}(A)$. Both FREYA's x and the
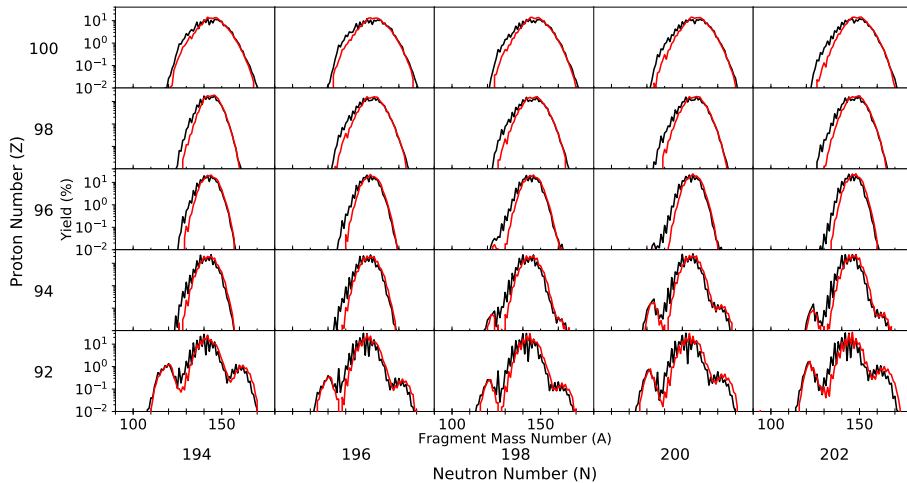
FIG. 3. (Color online) The fission product yields from neutron-induced fission at 0.1 MeV obtained from GEF (red) and FREYA (black). The increase in the predicted prompt neutron emission shown in Fig. 2 shifts the FREYA yields to lower mass number.

parameterized ratios in FIFRELIN and CGMF can reproduce the "sawtooth" shape of $\bar{\nu}(A)$ in gross or fine detail, depending on which approach is employed. The sawtooth shape is thought to arise from closed nuclear shells, in particular at $A = 132$ where there is a doubly closed shell and $\bar{\nu}(A)$ is at a minimum. This behavior occurs because closed-shell nuclei are harder to excite than highly deformed nuclei, resulting in fewer neutrons emitted. The x parameter in FREYA is, to a first approximation, based on giving more excitation energy to the fragments with masses below $A = 132$, and thus a higher neutron multiplicity for the light fragment, as suggested by data on well-studied nuclei such as ^{252}Cf(sf), ^{235}U(n,f) and ^{239}Pu(n,f) [59].

In the case of very neutron rich nuclei, the structure of $\bar{\nu}(A)$ is wholly unknown. Does the sawtooth effectively vanish if the fragment mass range is primarily between closed neutron shells at $N = 82$ and 126, as may be the case for some of the narrow symmetric splits seen in Fig. 1? In the case of a broad asymmetric split, one might even expect to see two "teeth" if the fragment range covers both closed shells. It is also not clear how the proximity of a closed proton shell might affect neutron emission. While FREYA will minimize $\bar{\nu}(A)$ in the proximity of a closed shell, even with $x = 1$ [60], forcing $x > 1$ in this region would artificially increase neutron emission, as seen in Fig. 2 for neutron-rich nuclei. As suggested earlier, one can take this difference in neutron emission as a theoretical uncertainty.

The increased neutron multiplicity in FREYA relative to GEF, as seen in Fig. 2 also has an effect on the shape of the fission product yields, as shown in Fig. 3. The fission product yields are shifted toward lower mass numbers for FREYA, demonstrating that more neutrons are emitted from the light fragments in FREYA than in GEF. We will

discuss the sensitivity of the r process to the energy sharing and de-excitation treatment later on. The sensitivity of the r process depends on how much isotopic material reaches the most neutron-rich region with $N > 184$ where FREYA predicts as many as ~ 3 more neutrons emitted per fission event than GEF.

Higher excitation energies could also change the relative neutron emission between GEF and FREYA. The GEF prescription gives more excitation energy to the heavy fragment and this energy flow increases with excitation energy. As energy is increased, the additional energy transferred to the heavy fragment increases $\bar{\nu}(A)$ on the heavy fragment side while leaving the light fragment neutron emission effectively fixed [26]. On the other hand, the energy sharing parameterizations of FREYA, CGMF and FIFRELIN instead increase the neutron multiplicities from the light and heavy fragments similarly so that $\bar{\nu}(A)$ rises monotonically with excitation energy [61]. Beta-delayed fission is a good test of the excitation energy dependence, as seen in Fig. 4. The excitation energy of this process can range from near zero, as is the case for spontaneous fission, up to $7 - 8$ MeV, as seen in the upper panel of Fig. 4, typically higher than the excitation energy of the neutron-induced fission energy relevant for the r process. The average neutron multiplicity in β-delayed fission, shown in the lower panel of Fig. 4, correspondingly tends to be higher than that of neutron-induced fission shown in the upper right panel of Fig. 2.

The β-delayed fission product yields predicted by GEF, given the average excitation energy for the β daughter shown in the upper panel of Fig. 4, also suggest that higher excitation energies will increase the asymmetry of the yields of neutron-rich nuclei. Compared to the case of neutron-induced fission shown in Fig. 1, even larger
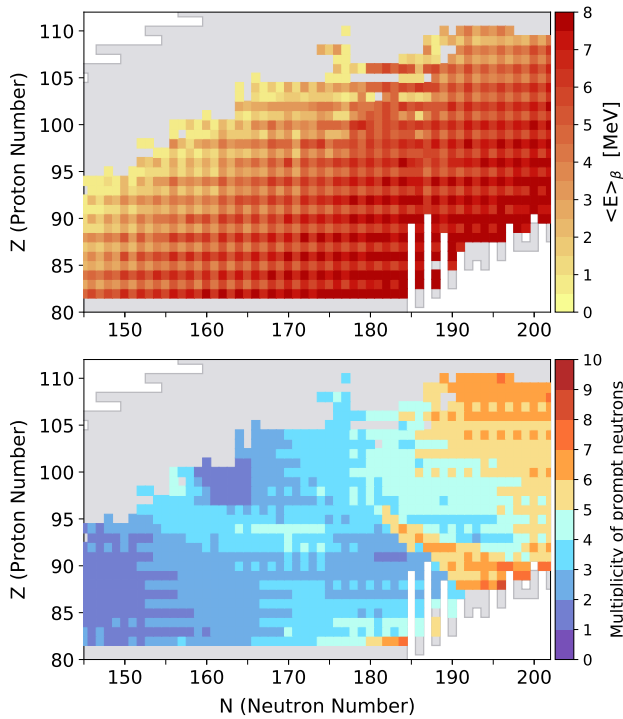
FIG. 4. (Color online) The average excitation energy for the daughter nucleus populated by β-decay [37] (upper panel) and the corresponding average prompt neutron emission as predicted by GEF when this excited daughter fissions (lower panel).

deviations from symmetry can be observed in the GEF β-delayed yields shown in purple in Fig. 5. For reference, the parameterized double-Gaussian fission yields of Kodama and Takahashi [21], widely used in r-process calculations, are also shown in Fig. 5 in green. These yields also show a transition from asymmetric to symmetric fission near neutron number $N = 184$, similar to GEF. However, in regions of the nuclear chart of interest for the r process, the broad distributions predicted by Kodama and Takahashi are centered near $A \sim 144$ for both asymmetric and symmetric fission while the asymmetric GEF yields tend to prefer $A \sim 150$ daughters. Although both models predict asymmetric yield contributions for similar nuclei, note that the GEF yields for such nuclei often contain a symmetric component as well.

III. IMPACT OF FISSION YIELD TRENDS ON r-PROCESS ABUNDANCES

For nucleosynthesis calculations, we use the network Portable Routines for Integrated nucleoSynthesis Modeling (PRISM) developed jointly at the University of Notre Dame and Los Alamos National Lab [14, 17, 37]. PRISM permits a straightforward implementation of mass model-dependent nucleosynthesis rates due to its flexibility with nuclear data inputs. For the masses of neutron-rich nuclei, we first apply the Thomas-Fermi (TF) model in order to employ masses and fission barriers consistent with the GEF inputs used to determine the yields. For this, we explicitly use the barriers assumed in GEF which include corrections to TF barriers, as discussed in Sec. II. Where available we use experimental masses [62] as well as experimentally established half-lives and branching ratios from NUBASE [63]. For theoretical α-decay rates we use the well-established Viola-Seaborg formula:

$$\log_{10}T_{1/2}^{\alpha}(s) = \frac{aZ + b}{\sqrt{Q_\alpha(\text{MeV})}} + cZ + d + h_{\log} \quad (1)$$

where we apply a least-squares fit to NUBASE2016 half-life data that takes into account the reported experimental uncertainties when optimizing coefficients. Using this procedure we find values of $a = 1.6606$, $b = -9.2990$, $c = -0.2121$, and $d = -32.5432$ as well as hindrance factors for unpaired neutrons of:

$$h_{\log} = \begin{cases} 0.5325, & Z \text{ odd, } N \text{ even} \\ 0.5253, & Z \text{ even, } N \text{ odd} \\ 0.9222, & Z \text{ odd, } N \text{ odd} \end{cases} \quad (2)$$

We use neutron capture, β-decay, neutron-induced fission and β-delayed fission rates as in Refs. [37, 65–68], with all rates determined from the same model masses as in Ref. [69] and updated to be self-consistent with the fission barrier heights of a given model. For spontaneous fission we apply a parameterized prescription with a simple dependence on barrier height as in Refs. [70, 71]. Therefore with the same fission barriers used to determine the fission yields and rates of all fission reaction and decay channels, our calculations which apply TF inputs represent the most fully self-consistent fission cycling r-process calculations in this work.

For astrophysical conditions, we consider dynamical ejecta from a 1.2–1.4 $M_\odot$ neutron star merger simulation [72, 73] for which we calculate nuclear reheating self-consistently with the chosen nuclear inputs when extrapolating beyond the reported simulation trajectory (with an assumed 50% heating efficiency). We extrapolate the density by assuming free expansion as in Korobkin *et al.* [74] and assume nuclear statistical equilibrium (NSE) at 10 GK to obtain seed nuclei abundances using the SFHo equation of state [75]. Since these simulation trajectories are publicly available, we refer to the original number labeling (1–30) in order to permit direct comparisons with the results presented here. We first consider a "cold", very neutron-rich ($Y_e = 0.01957$) tidal tail trajectory in this set (traj. 1) which permits significant fission cycling due to its extreme neutron richness. Here the term "cold" when used in reference to an astrophysical trajectory implies photodissociation drops out of equilibrium early, leaving β-decay to compete with neutron capture. In contrast the term "hot" when applied to trajectories implies conditions which support an extended $(n,\gamma) \rightleftharpoons (\gamma,n)$ equilibrium.
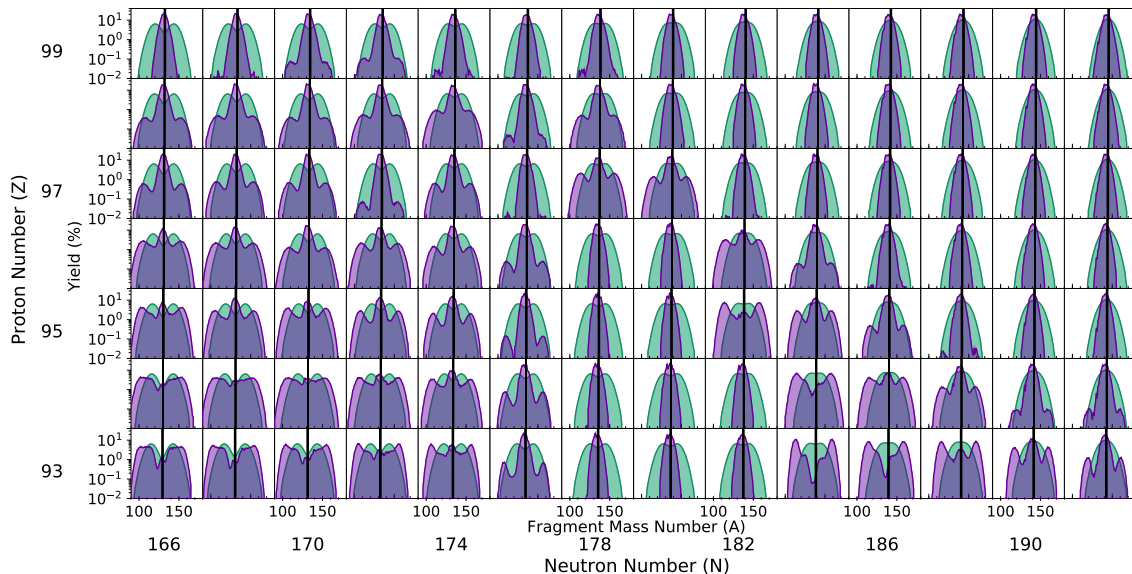
FIG. 5. (Color online) The product yields predicted for the fission of a daughter nucleus populated by β-decay (purple) after using the excitation energies shown in Fig. 4 in GEF as compared to the yields from Kodama and Takahasi [21] (green) and simple symmetric splits (black).
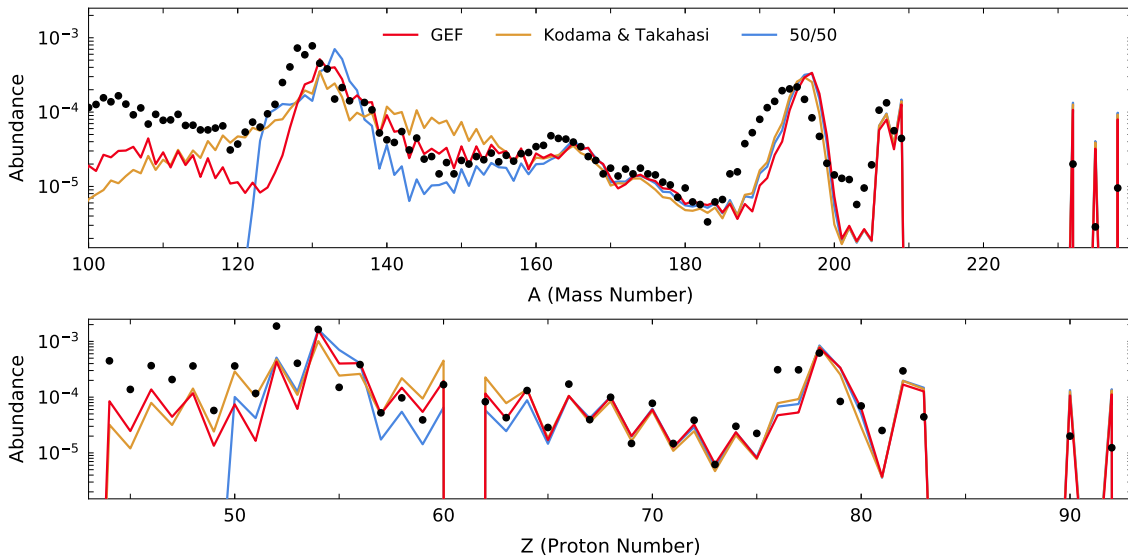

FIG. 6. (Color online) The r-process abundances at 1 Gyr using GEF yields for spontaneous fission, neutron-induced fission and β-delayed fission (red) as compared to using the fission yields of Kodama and Takahasi (gold) and simple symmetric splits (blue). The solar data is that of Sneden *et al.* [64].

We show the impact of the asymmetric-to-symmetric yield trends predicted by GEF as compared to more simplistic descriptions in such fission rich environments in Fig. 6. The underproduction at $A \sim 144$ seen with a simple symmetric split (50/50) is a consequence of their narrow distribution which exclusively deposits material near $A \sim 130$ when r-process material encounters the re-

gion with $Z \gtrsim 90$ at $N < 184$. In contrast, the fission yields of Kodama and Takahashi, whose r-process impact has been previously explored in Refs. [15, 22, 37], are exclusively asymmetric at $N < 184$ and transition to symmetric distributions at higher neutron number (see Fig. 5). However the width of these fission yields places material over a fairly broad range around $A \sim 144$ at both
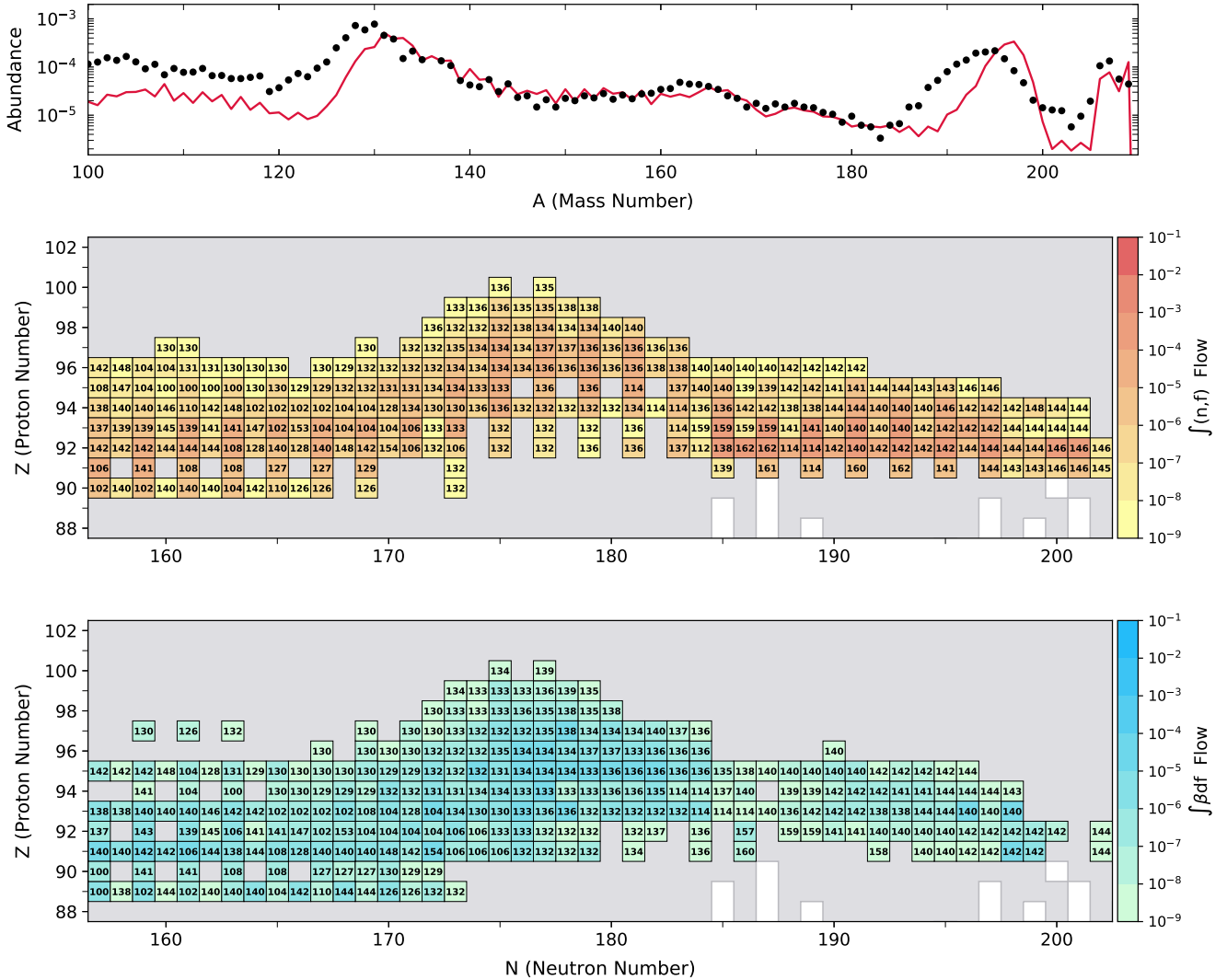
FIG. 7. (Color online) The fission flow ($\lambda_i Y_i$ where λ_i is the rate of the reaction or decay and Y_i is the abundance) for nuclei undergoing neutron-induced (middle panel) and β-delayed (lower panel) fission integrated over time along with the resultant r-process abundance pattern (upper panel). The numbers labeling nuclei in middle and lower panels denote the mass number at the location of the maximum of the daughter fission yield distribution (here from GEF).

early and late times. The overproduction of the light lanthanides with the Kodama and Takahashi yields is a direct consequence of its global preference for $A \sim 144$ fission daughters. The results obtained with the GEF yields here predict a more gradual fall off for the right edge of the second r-process peak, and the lanthanide abundances in this region, as well as near $A \sim 150$, follow solar data trends. This lanthanide abundance behavior given the GEF yields is due to the transition from asymmetric to symmetric yields discussed in Sec. II. The inclusion of prompt neutron emission with GEF as compared to no neutron emission with simple symmetric splits or Kodama and Takahashi has less influence. An effect of prompt neutron emission can be seen by examining the location of the second peak maximum when using the

GEF yields as compared to symmetric splits. Neutron emission shifts the GEF fission yields to lower mass numbers relative to symmetric distributions without neutron emission (recall Fig. 5) giving an r-process second peak located at $A = 131$ as compared to $A = 133$ with simple splits. Additionally, the fission neutrons produced by GEF narrow the third peak relative to distributions without neutron emission, as can be seen in Fig. 6.

To explicitly demonstrate the role that GEF yield trends play in determining the r-process abundance pattern, the integrated fission flow can be cross checked with the fissioning daughter yields for these nuclei as shown in Fig. 7. Here we label each reactant species at Z, N with the mass number which locates the maximum of the fission yield for the fissioning nucleus Z_f, N_f

(where $Z_f = Z + 1$, $N_f = N - 1$ for βdf and $Z_f = Z$, $N_f = N + 1$ for (n,f)). In the case of symmetric yields, the mass number, A, in the boxes of Fig. 7 will be $A \sim (N_f + Z_f)/2$, where N_f and Z_f correspond to the fissioning nucleus populated from the reactant species at Z, N. If the fission is asymmetric, the mass number shown is for one fragment peak so material will be deposited at $A' \sim (N_f + Z_f) - A$ as well. Of course the yields can contain both symmetric and asymmetric contributions that are similarly probable. However, it is still instructive to see explicitly where each fissioning nucleus will preferably deposit material. With the GEF yields, the r-process material in "cold" dynamical ejecta trajectories, as in the very neutron-rich tidal tail ejecta conditions of Fig. 6, first encounters symmetric yields centered at $A \sim 144$ beyond the $N = 184$ shell closure. Significant fission flow passes through this region as neutron-induced fission acts to terminate the r process. As material decays back to stability, nuclei at neutron numbers below $N = 184$ with substantial asymmetric yield contributions are encountered, placing material primarily near $A \sim 110, 130$, and 150. The contributions from fission products at early times near $A \sim 144$, followed by late-time contributions near $A \sim 130, 150$, work to smooth the right edge of the second r-process peak. It is interesting to note that with the GEF yields there are only a few nuclei with $A \sim 160$ fission daughters which place material directly into the rare-earth peak region. Therefore, with these yields it is not possible to explain rare-earth peak formation by a late-time deposition of fission material at $A \sim 164$, as can occur with the four hump fragment distributions predicted by the SPY yield model [19].

The effect of using distinct sets of fission yields for spontaneous, neutron-induced, and β-delayed fission further demonstrates the sensitivity of the r process to the asymmetries present in GEF yields, as shown in Fig. 8. Here we consider merger dynamical ejecta trajectory 22 with $Y_e \sim 0.054$ which starts similarly cold to traj. 1 but later reaches higher temperatures. In such conditions, the enhanced asymmetries in the fission yields discussed in Sec. II (and shown in Fig. 1) due to an excited compound parent nucleus places more material at $A \sim 110$ and 150 as compared to the case when all fission processes make use of spontaneous fission yields. These enhanced asymmetric contributions produce a clear signature in the final abundance pattern with the fission yields which account for excitation energy giving a result more consistent with observed solar data.

The influence of the fission fragment energy sharing and de-excitation treatment, which determines prompt neutron emission, is demonstrated by the r-process abundances using the FREYA fission product yields as compared to those from GEF, shown in Fig. 9. Here we again consider the astrophysical conditions of traj. 22 so that the influence of the de-excitation and energy sharing treatment can be directly compared to the impact from using excitation energy dependent sets of fission yields as in Fig. 8. The effect of the systematically higher neutron
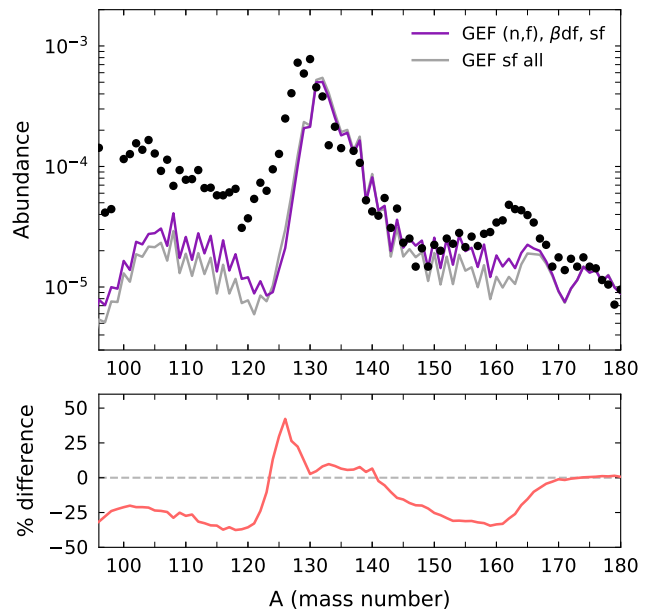

FIG. 8. (Color online) The abundance of the second r-process peak when the GEF yields for spontaneous fission are applied to all fission processes (grey) as compared to results using GEF spontaneous, neutron-induced, and β-delayed fission yields for their respective reaction channel (purple) (upper panel) along with the percent difference between these results (lower panel).

emission predicted by FREYA on the r-process abundance pattern is two fold. The widening of the yield distributions toward lower mass number that accompanies increased neutron emission places more material to the left of the $N = 82$ shell closure. This can lead to an increase on the order of 10% in the height of the second peak. The increase of material held at the $N = 82$ shell closure effectively decreases the number of available isotopes that can neutron capture back up past the $N = 126$ shell closure which therefore reduces overall actinide abundances by $\sim 10\%$. The tendency of FREYA yields to decrease the ability of material to access the heaviest nuclei also implies less fission activity in the region of mostly asymmetric yields between $N = 126$ and $N = 184$ which leads to less lanthanide material at $A \sim 150$. The widening of the yields toward lower mass number is primarily responsible for the differences seen between GEF and FREYA. However, the influence of the extra neutrons alone can be seen from the overall shift in the pattern to the right of the rare-earth peak toward higher mass number. Such a narrowing of the third r-process peak due to late-time neutron capture from β-delayed neutron emission and prompt neutron emission from excited fission fragments has been noted in previous work [15, 18, 74]. Although the energy sharing and de-excitation treatment can lead to differences in the main r-process peaks, these effects are modest relative to the
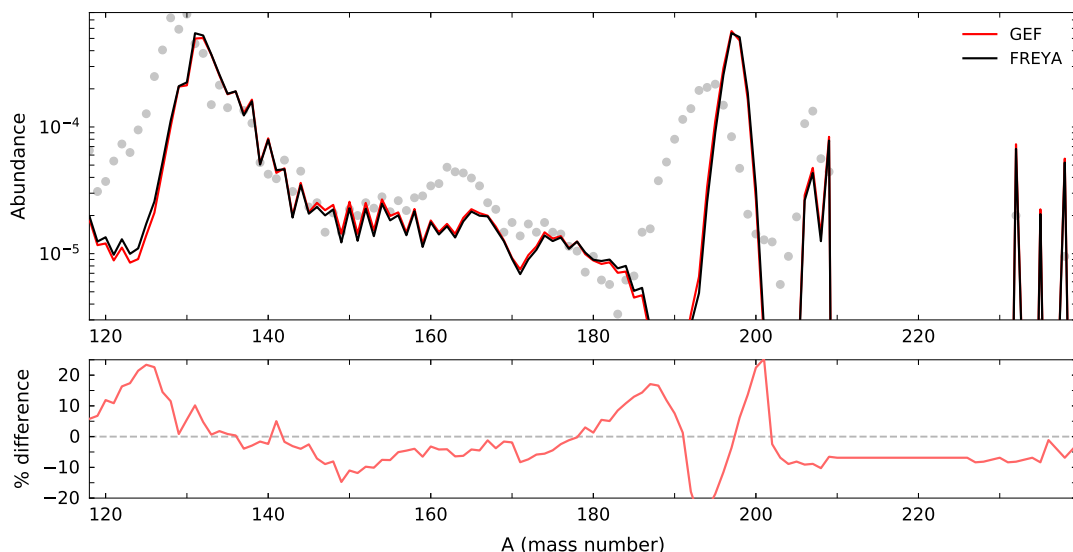
FIG. 9. (Color online) An example of the r-process abundance pattern sensitivity to the fission fragment energy sharing and de-excitation treatment from examining results using GEF (red) as compared to FREYA (black).

influence of the global yield trend demonstrated in Fig. 6, which points to the fragment yields (prior to neutron emission) as being of primary importance for r-process calculations.

We next consider the effect of more realistic fission yields and prompt neutron emission, as calculated by GEF and FREYA, on the nuclear heating rates needed to calculate kilonova light curves. For such heating rate calculations, we use the "cold" dynamical ejecta conditions applied in Figs. 6 and 7. We calculate the heating contributions from β-decay, neutron capture, β-delayed fission, and neutron-induced fission as flow $\times$ Q-value for each channel and compare the results using GEF and FREYA to simpler treatments in Fig. 10. We first focus on the heating before ~ 1 day when β-delayed and neutron-induced fission are most active. Both the β-decay and β-delayed fission show some dependence on the yield distribution, however it is the neutron capture reaction channels that show a rather pronounced sensitivity to the fission yields. Applying simple symmetric splits produces early time heating contributions from neutron capture and neutron-induced fission which are about three orders of magnitude lower than those predicted using the GEF yields. This difference comes from the tendency of symmetric splits to deposit material in a concentrated region near the $N = 82$ shell closure as compared to the wider distribution of daughter products seen with GEF. The late-time addition of nuclei to the right of the $N = 82$ shell closure permits further neutron capture and therefore more material is driven up in mass number toward the fissioning regions near $N = 184$, correspondingly increasing the heating contribution from neutron capture and neutron-induced fission. A comparison of heating rates when using the

yield model of Kodama and Takahashi, which does not contain a prescription for neutron emission from excited daughter fragments, confirms that it is the narrow placement of daughter nuclei near $N = 82$ that is most responsible for the lower heating rate for neutron-induced processes in the symmetric yield case. The inclusion of prompt neutron emission from the excited fragments as in GEF can further increase the heating from neutron capture reaction channels by a factor of around three as compared to Kodama and Takahashi. We note that applying the yields obtained using the FREYA energy sharing and de-excitation treatment, while not shown in Fig. 10, can further increase the heating from neutron capture processes by roughly 10% at these early times.

When timescales on the order of days or longer are considered, the influence of the fission treatment on nuclear heating becomes more pronounced due to the late-time dominance of fission, specifically the spontaneous fission of ^{254}Cf [17]. Fig. 11 shows the heating rate for β-decay, spontaneous fission, and α-decay when the yield distributions from GEF and FREYA are compared with those obtained using simple symmetric splits. The 50/50 splits result in the largest predicted late-time dominance of the spontaneous fission heating with the greatest deviation between β-decay and spontaneous fission heating curves. The spread of fission recycled material produced by the GEF yields can produce nuclei closer to the neutron dripline where β-decay rates are faster, thereby increasing the total effective β heating. When considering the extra late-time neutrons and increased yield widths predicted by FREYA, Fig. 11 shows that α-decay and spontaneous fission heatings are decreased relative to the GEF case with slightly more material getting stuck near $N = 82$ and therefore less material populating the high-
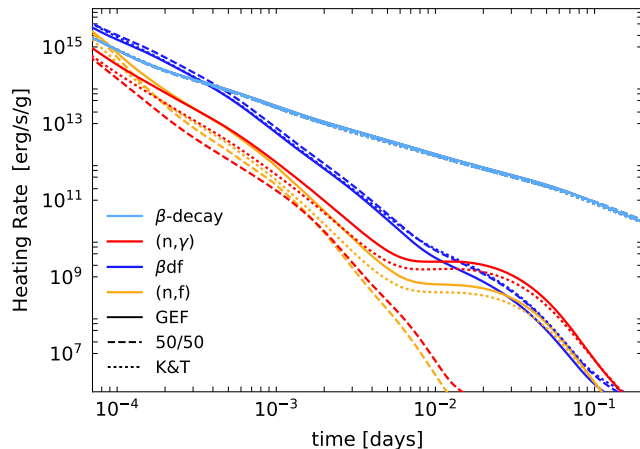
FIG. 10. (Color online) The nuclear heating rates for β-decay (blue), β-delayed fission (light blue), neutron capture (red) and neutron-induced fission (orange) as a function of time using GEF fission yields (solid lines) as compared to results using simple symmetric splits (dashed lines) and the yields of Kodama and Takahashi (dotted lines). The masses and fission barriers applied are those of TF and GEF respectively.
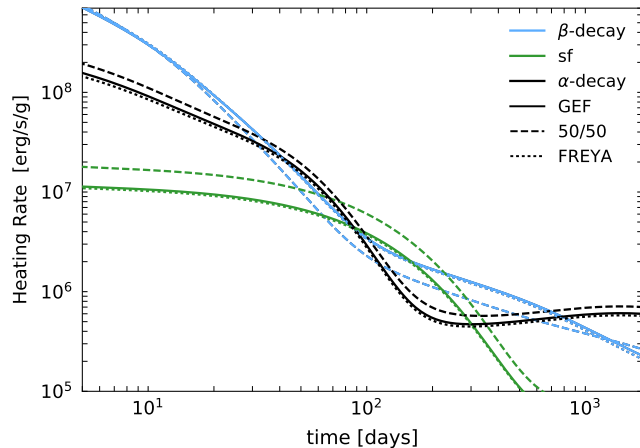

FIG. 11. (Color online) The nuclear heating rate for β-decay (blue), alpha decay (black) and spontaneous fission (green) as a function of time using GEF fission yields (solid lines) as compared to results using simple symmetric splits (dashed lines) and the yields with the FREYA energy sharing and de-excitation treatment (dotted lines). The masses and fission barriers applied are those of TF and GEF respectively.

est mass number regions (Fig. 9). Figures 10 and 11 explicitly demonstrate that in fission cycling conditions the exact details of the heating rates applied to calculations of kilonova light curves depends on the nuclear physics assumptions for the heaviest, fissioning r-process nuclei.

As described above, exactly how fission yields shape abundance patterns and heating curves depends sensi-tively on which nuclei are fissioning. This is in part set by the r-process astrophysical conditions. To examine this sensitivity, we consider astrophysical conditions from the same 1.2–1.4 $M_\odot$ neutron star merger simulation [72] used throughout this section. While all thirty of these dynamical ejecta trajectories are similarly neutron-rich, with Y_e ranging from $\sim 0.015 - 0.055$, they exhibit a variety of density and temperature profiles. A compar-ison of the final abundances (upper panel), abundance wighted mass number (middle panel), and temperature profile (lower panel) for the two trajectories found to rep-resent the extremes in temperature evolution can be seen in Fig. 12. In contrast with the "cold" conditions of tra-jectory 1, in the "hot" dynamical ejecta conditions of tra-jectory 17, the r-process path does not significantly popu-late the mostly symmetric yield region past $N = 184$ and therefore underproduces near $A \sim 140$ relative to results with cold conditions. This is partially due to the ability of photodissociation to prevent material from reaching the most neutron-rich nuclei past $N = 184$ but also due to the slightly higher Y_e (~ 0.049) producing somewhat lower fission flow (total integrated fission flow for traj. 17 of 0.00488 as compared to 0.00567 for traj. 1). The region below $N = 184$ with mostly asymmetric yields, however, is still accessed in such hot conditions result-ing in increases to the abundances near $A \sim 100, 150$ (to show this behavior explicitly the version of Fig. 7 given the astrophysical conditions of traj. 17 used in Fig. 12 has been included in Supplemental Materials). Therefore which fissioning nuclei are accessed is influenced by the impact of the astrophysical conditions on the location and termination point of the r-process path.

IV. VARIATIONS IN OTHER NUCLEAR INPUTS INFLUENCING FISSION DEPOSITION

Having established that the location and termination point of the r-process path influences which fissioning nuclei will be most impactful in the r process, we next consider how other nuclear inputs, such as the nuclear masses, fission barriers, and β-decay rates, can affect the nuclear flow. The connection between the path termi-nation point and the fission yields most influencing r-process abundances has been made previously. For ex-ample, in Ref. [23] the authors find that termination near $N = 184$ results in depositions of daughter nuclei from mostly asymmetric yields while higher mass number ter-mination points see more influence from the symmetric yields of high mass nuclei. Here we explore such consider-ations by examining the termination behavior predicted by different mass models. We show that it is not only how far the r-process path proceeds, but also the struc-ture of predicted fission barriers near $N = 184$, which determine the fission yields of most relevance.

To study these dependencies, we compare re-sults when employing the Finite Range Droplet Model (FRDM2012), Thomas-Fermi (TF), Hartree-Fock-
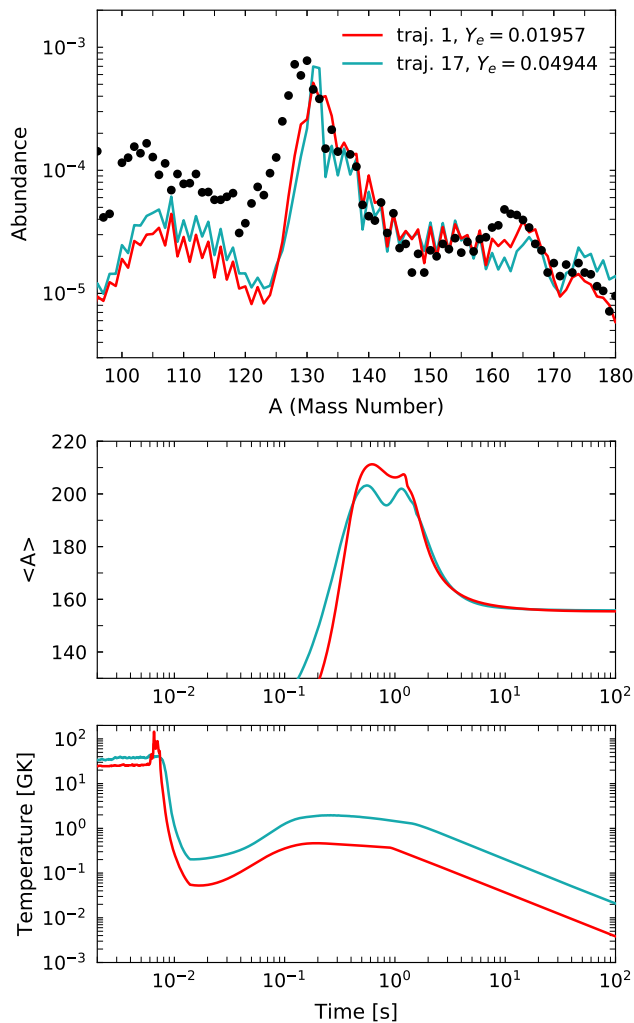
FIG. 12. (Color online) The r-process abundance pattern (upper panel) given two dynamical ejecta trajectories from a 1.2–1.4 $M_\odot$ neutron star merger simulation [72] (lower panel) along with the abundance weighted mass number as a function of time for each set of conditions (middle panel).

Bogoliubov (HFB-17), and Extended Thomas-Fermi with Strutinsky Integral (ETFSI) mass models. All reaction and decay rates are consistently calculated with model masses as in Ref. [69] and all fission rates are updated based on the fission barrier heights of a given model. The fission barriers are illustrated in Fig. 13. The barriers for the Finite Range Liquid Droplet Model (FRLDM) are from [76, 77], Thomas-Fermi barriers are again considered to be those applied in GEF, and ETFSI barriers taken from [78, 79]. The HFB-14 fission paths used to determine the barriers are available for $Z \geq 90$ in the BRUSLIB database [80] as well as TALYS. We chose these four models since the data for both the masses and fission barriers consistent with model masses are publicly available and commonly used in r-process calculations. For the fission yields in this section, we apply the

default GEF distributions presented in Sec. II and do not update these to reflect the barriers of each model. With a fixed fission yield model, we can study how the abundance pattern is shaped by these yields when different sets of fissioning nuclei, as determined by the fission barriers, are accessed.

We first consider "cold" dynamical ejecta conditions as in Ref. [7] without nuclear reheating in order to examine the case in which the nuclear flow can reach the highest possible mass numbers because it is less impeded by photodissociation. The black outline in Fig. 13 shows the location of the most populated nuclei (abundance $\geq 10^{-10}$) just before the r-process path begins to move back toward stability (taken to be the time when the abundance weighted mass number reaches its last maximum). With FRDM and TF, material encounters relatively low barrier heights $\sim 4 - 5$ MeV as it pushes past the $N = 184$ shell closure, permitting fission to occur quickly and thus preventing the nuclear flow from continuing much higher in mass number. As noted in Ref. [15], we find HFB permits the synthesis of heavier nuclei than FRDM and TF models due to higher barriers near the predicted $N = 184$ shell closure. The same is true for the ETFSI model [22, 33], which was previously found to have its nuclear flow terminated by β-delayed fission [33] instead of neutron-induced fission which terminates the path using TF and FRLDM barriers. We also find β-delayed fission to be more active in the ETFSI case, with a $\sim 60\%$ enhancement in the total integrated β-delayed fission flow relative to the flow found with TF or FRDM. We note that the ability to synthesize nuclei with higher mass number makes r-process calculations using ETFSI and HFB models more sensitive than results with FRDM and TF to the increase in prompt neutrons and widening of yields predicted by FREYA which become more significant at higher neutron and proton numbers (as shown in Figs. 2 and 3) (to show this explicitly the version of Fig. 9 given the astrophysical conditions of traj. 22 with HFB model inputs has been included in Supplemental Materials).

The corresponding final abundance pattern given the evolution of the nuclear flow shown in Fig. 13 is presented in Fig. 14. The ability of ETFSI and HFB-17 to reach nuclei higher in mass number due to higher fission barriers near $N = 184$ means these models access more of the region found by GEF to have mostly symmetric yields centered at $A \sim 144$ as compared to the nuclei accessed by FRDM and TF. We find that the higher nuclear flow through the symmetric GEF yield region with ETFSI and HFB, seen in Fig. 14, contributes to their overproduction of the right edge of the second peak as compared to solar data. The model dependent shell closure predictions also play a role with FRDM having a stronger $N = 82$ shell closure than ETFSI and HFB which keeps fission daughter products closer to the $A \sim 130$ region at late times. It is therefore the interplay between the barrier height landscape around $N = 184$ and the structure of the $N = 82$ shell closure which determines the shape of the second
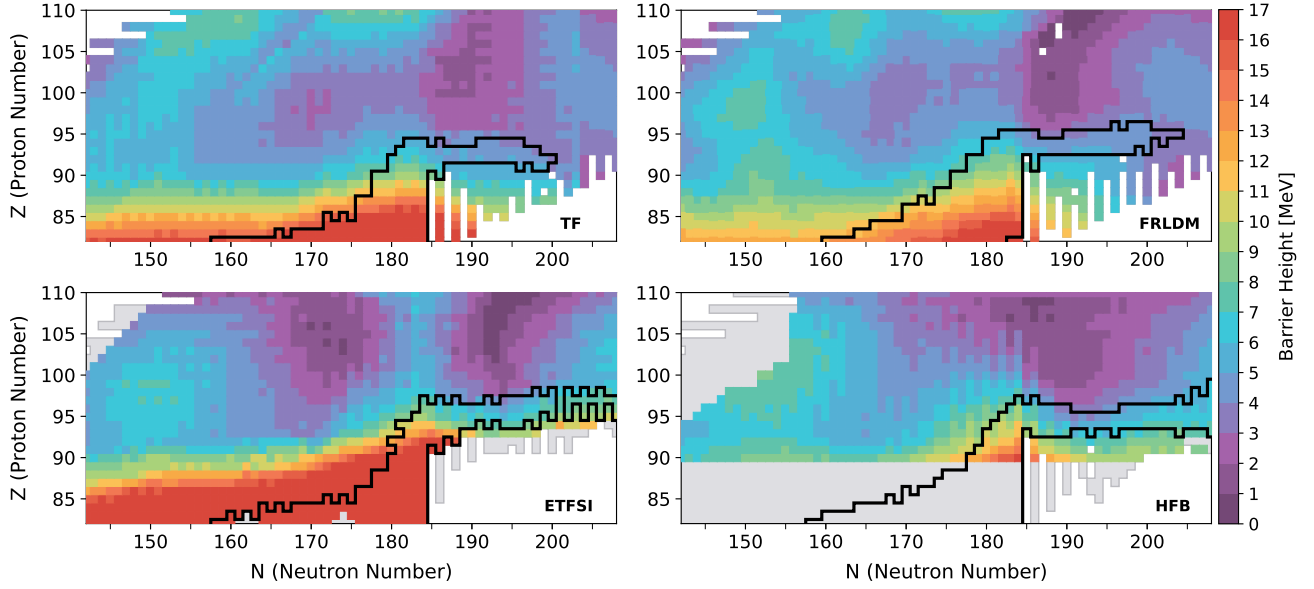
FIG. 13. (Color online) Fission barrier heights for GEF (TF) (upper left), FRLDM (upper right), ETFSI (lower left) and HFB-14 (lower right) models along with a snapshot of the r-process material with an abundance $\geq 10^{-10}$ (black outline) just before the r-process path begins to move back toward stability in cold, dynamical ejecta conditions without nuclear reheating.
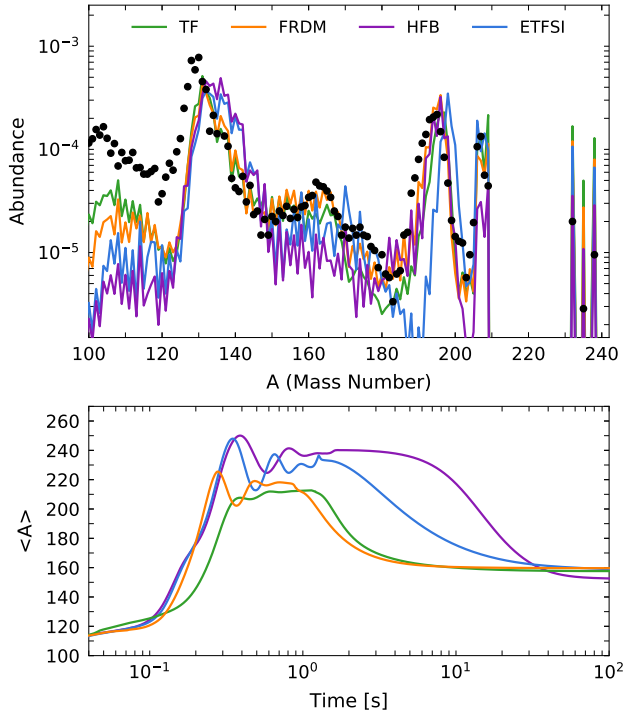

FIG. 14. (Color online) (Upper panel) The r-process abundances at 1 Gyr using GEF fission yields along with reaction rates determined by the masses (barriers) of TF (GEF) (green), FRDM2012 (FRLDM) (orange), ETFSI (ETFSI) (blue), and HFB-17 (HFB-14) (purple) models. (Lower panel) The abundance weighted mass number as a function of time for each of the four mass models considered.

r-process peak in fission cycling conditions. It was previously found in Ref. [15] that given HFB-14 barriers, most of the fissioning nuclei accessed had fission fragments lying between $A = 125$ and $A = 155$, similar to their results with the FRDM case. We find that the HFB-14 barriers produce fission flow which dominantly accesses fragment distributions centered at $132 \leq A \leq 150$, even after material is primarily located at $N < 184$. This contributes to the overall shift in the second r-process peak with HFB in Fig. 14 (to show this explicitly the version of Fig. 7 given the astrophysical conditions of traj. 1 and HFB model inputs has been included in Supplemental Materials).

We next turn to results given dynamical ejecta conditions which include self-consistent nuclear reheating. We recalculate the thirty trajectories of the 1.2–1.4 $M_{\odot}$ neutron star merger simulation [72] considered in Sec. III with the four sets of mass and barrier models described above. The results appear in Fig. 15. Although these dynamical ejecta trajectories are all very neutron-rich, the variations in their density and temperature profiles cause a spread in the range of predicted abundances along the right edge of the second peak. As previously discussed in the context of Fig. 12, this is largely due to whether material reaches the region past $N = 184$ where GEF yields are mostly symmetric and deposit material near $A \sim 144$. Another difference in the abundance patterns is the width of the $A \sim 195$ peak, which is controlled by the amount of late-time neutron capture. Trajectories with more reheating tend to produce a narrower peak.

Having considered the role of masses and fission barriers, we next turn to how β-decay rates influence which
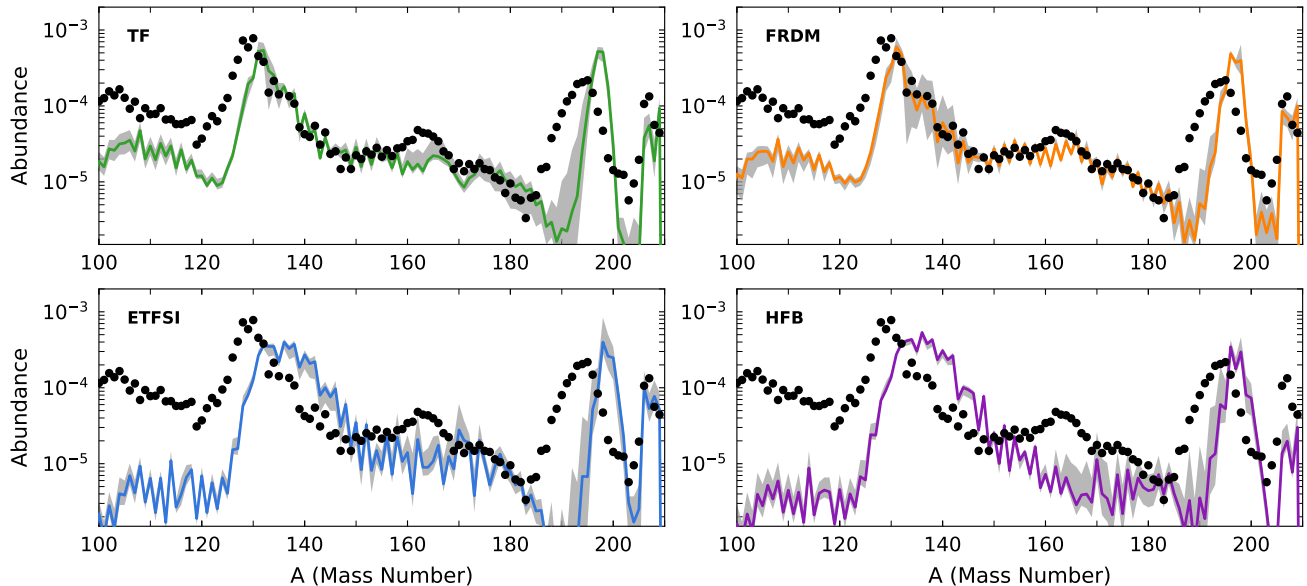
FIG. 15. (Color online) Range (grey band) and average (colored line) for the final r-process abundances with TF (upper left), FRDM (upper right), ETFSI (lower left) and HFB (lower right) models given thirty 1.2–1.4 M$_\odot$ neutron star merger simulation trajectories [72].
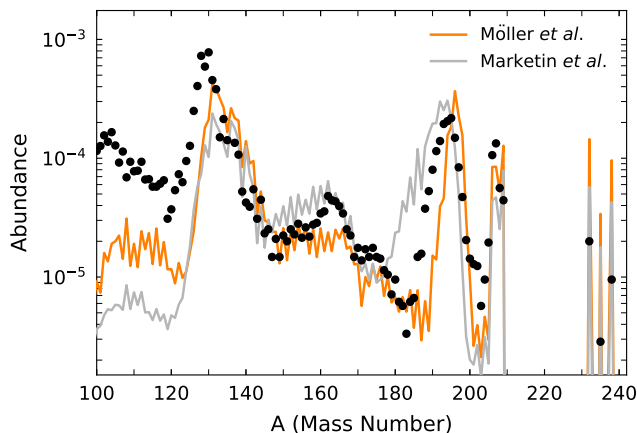

FIG. 16. (Color online) The r-process abundances at 1 Gyr using the cold tidal tail conditions of trajectory 1 [72] and the FRDM2012 mass model with β-decay rates determined from Möller et $al.$ QRPA calculations [68] (orange) as compared to those from Marketin et $al.$ [81] (grey).

fissioning nuclei are accessed in an r-process calculation. We repeat the FRLDM/FRDM simulations described above with the Möller et $al.$ [68] β-decay rates replaced by those from Marketin et $al.$ [81] and show an example abundance pattern comparison in Fig. 16. The two sets of rates are generally similar except for nuclei above the $N = 126$ shell closure, where the Marketin et $al.$ rates are faster. Simulations with the faster Marketin et $al.$ rates tend to show less material hung up in the higher

mass regions than with Möller et $al.$ rates which reduces the extra post-freeze-out neutrons produced via fission and β-delayed neutron emission. This in turn thwarts the shifting and narrowing of the third peak from late-time neutron capture (as noted in Refs. [15, 22]). This reduction of nuclei present near $N = 184$ hinders the opportunity for fission to build and shape the second r-process peak at late times. Specifically, with nuclei near $N = 184$ is less populated at freeze-out, the region of the nuclear chart where GEF predicts fission yields to be centered mostly near $A \sim 130$ is not accessed very heavily. This is responsible for the differences in the height of the second r-process peak when results using the Möller et $al.$ [68] and Marketin et $al.$ rates are compared (to show this explicitly the versions of Fig. 7 given the Marketin et $al.$ and Möller et $al.$ conditions applied in Fig. 16 have been included in Supplemental Materials).

We lastly consider how the masses and fission barriers influence the sensitivity of the nuclear heating rates to fission yield treatments. To do so we repeat the calculations presented in Sec. III with nuclear rates determined from FRDM2012 masses and FRLDM fission barriers, shown in Figs. 17 and 18. Figure 17 confirms that the three order of magnitude discrepancy in the heating for neutron capture channels when 50/50 and GEF yield results are compared is not isolated to the TF model. This increase in neutron-induced fission in the GEF case is even stronger given FRDM inputs (compare Figs. 10 and 17) since here the rise in heating rate of neutron capture channels reaches a value one order of magnitude lower than the dominant β-decay heating channel.

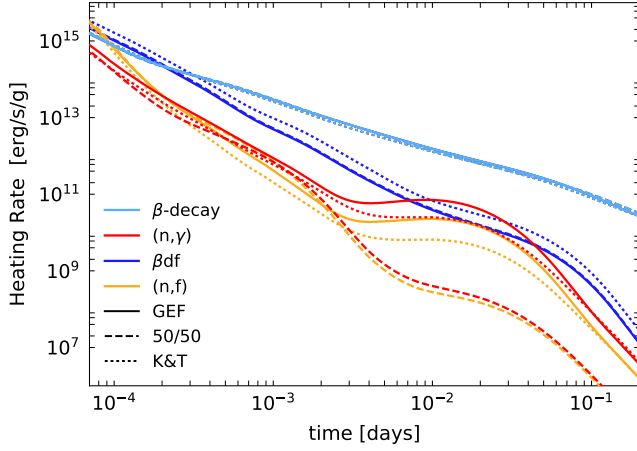When late time heating is considered, a comparison of

FIG. 17. (Color online) The nuclear heating rates for β-decay (blue), β-delayed fission (light blue), neutron capture (red) and neutron-induced fission (orange) as a function of time using GEF fission yields (solid lines) as compared to results using simple symmetric splits (dashed lines) and the yields of Kodama and Takahashi (dotted lines). The masses and fission barriers applied are those of FRDM2012 and FRLDM respectively.
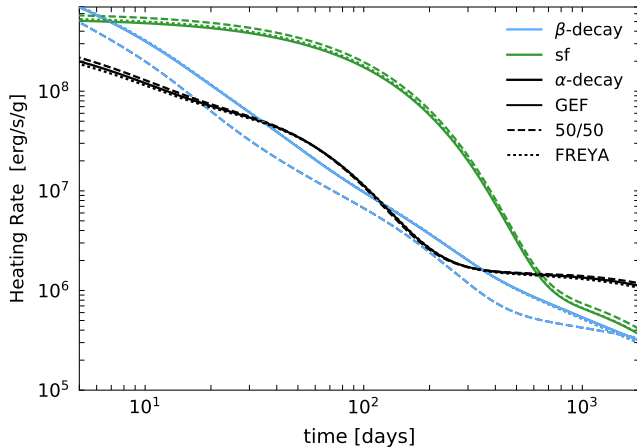

FIG. 18. (Color online) The nuclear heating rate for β-decay (blue), alpha decay (black) and spontaneous fission (green) as a function of time using GEF fission yields (solid lines) as compared to results using simple symmetric splits (dashed lines) and the yields with the FREYA energy sharing and de-excitation treatment (dotted lines). The masses and fission barriers applied are those of FRDM2012 and FRLDM respectively.

Figs. 11 and 18 shows that the spontaneous fission contribution to the late-time nuclear heating is two orders of magnitude larger with the FRDM masses and FRLDM barriers as compared to the result using TF masses and GEF barriers. In Fig. 19 we show that it is the difference between the barriers of these two models along the

$A = 254$ isobaric chain that is primarily responsible for the difference in the late-time contributions of this long-lived californium nucleus. We find that in this region of the nuclear chart, fission flows are highest in the presence of barrier heights around $4 - 5$ MeV. In the TF model, this is precisely the height of the barrier which $A = 254$ nuclei must overcome in order to eventually populate californium, and we find fission of these nuclei transfers material out of this isobaric chain. In contrast, with the FRLDM model, the nuclei set to populate ^{254}Cf pass just to the left of the region with barrier heights of $4 - 5$ MeV and the fission encountered along the path to ^{254}Cf is insignificant. Note from the discussion in Sec. II that the GEF barriers include some systematic corrections in this region of the nuclear chart. However, along the $A = 254$ isobaric line, the TF barriers without GEF corrections are also $4 - 5$ MeV or lower. Specifically we find that the lower barriers of TF/GEF roughly translate into an order of magnitude higher neutron-induced fission rate for two key nuclei (^{254}Np and ^{255}U) along the path feeding ^{254}Cf. Though these two key nuclei are populated late in the r process (on the order of $\sim 1 - 10$ seconds) when the neutron abundance has dropped significantly, their neutron-induced fission rates can be sufficiently high to interrupt the β feeding of ^{254}Cf. We do not find the differences in β-delayed fission with TF and FRDM models to significantly affect the population of ^{254}Cf.

Finally, we comment on the population of ^{254}Cf given all the nuclear mass/fission barrier models considered in this section. The ^{254}Cf abundance as a function of time for all cases is shown in Fig. 20. The two order of magnitude reduction in the abundance of this nucleus with the TF model relative to FRDM is expected given the differences in barrier heights and fission rates previously discussed. The ETFSI model also populates ^{254}Cf less than FRDM. In this case, the barrier height landscape near $N = 184$ leaves less material available to populate ^{254}Cf when it pushes significantly past this predicted shell closure. After fission terminates the flow of material near $N = 210$, the significant amount of material piled up here encounters the right edge of a large region with low barriers and fissions quickly. In addition, the ETFSI model predicts the ^{254}Cf path to encounter a small region of barriers with heights $4 - 5$ MeV which reduce the population β feeding this nucleus. Much like ETFSI, the HFB model barriers allow a significant flow of material past $N = 184$ which will then not be available to populate the $A = 254$ isobaric chain. However the material that remains piled up near $N = 184$ at freeze-out which is capable of populating ^{254}Cf is not inhibited by low $4 - 5$ MeV barrier heights during its decay back to stability. This produces a higher predicted ^{254}Cf abundance with HFB as compared to ETFSI and TF models. We find that it is the FRDM model which populates ^{254}Cf most strongly through the coupled effects of low barriers just past $N = 184$ preventing material from moving to higher mass number as well as sufficiently high barriers along the ^{254}Cf path that prevent a significant depopulation from
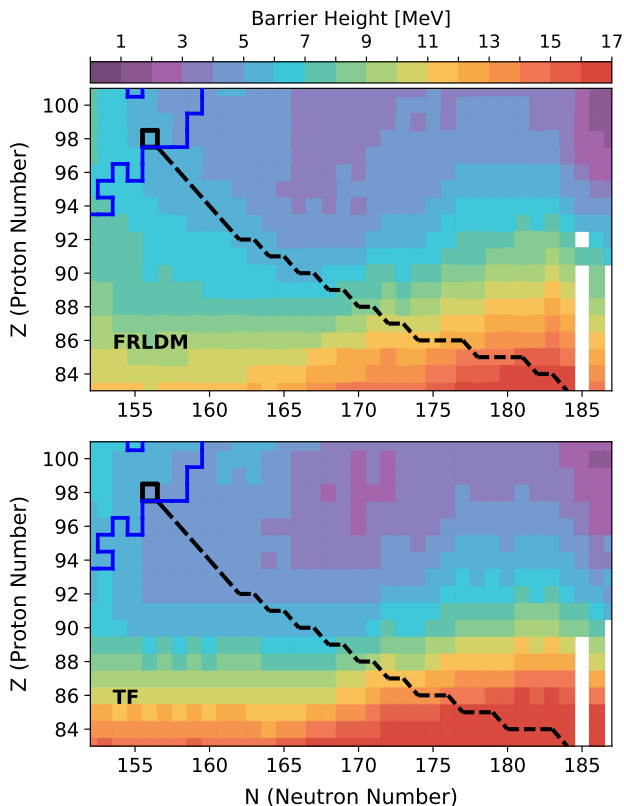
FIG. 19. (Color online) Fission barrier heights for FRLDM (upper panel) and GEF (TF) (lower panel) along with the β-decay path for ^{254}Cf in each case (black dashed line). The blue outline shows the region of experimentally established decay rates.
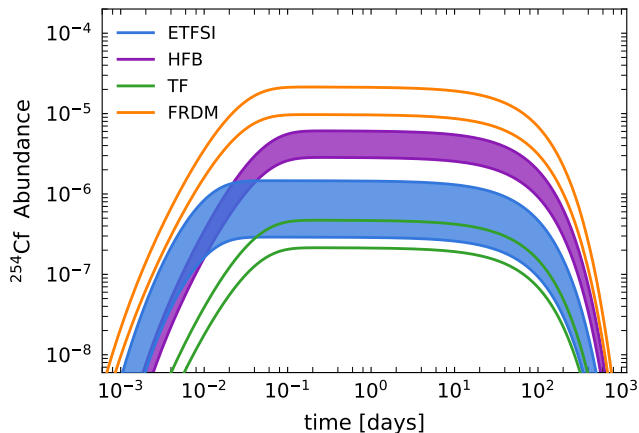

FIG. 20. (Color online) The ^{254}Cf abundance as a function of time with TF (green), FRDM (orange), ETFSI (blue) and HFB (purple) models. The bands represent the range in ^{254}Cf production given thirty 1.2–1.4 M$_\odot$ neutron star merger simulation trajectories [72].

fission. It is clear that the fission barrier heights of heavy unstable nuclei are key to assessing the influence of ^{254}Cf on kilonova light curves. Therefore, potential observations of the increased light curve luminosity associated with the heating "bump" from ^{254}Cf at late times would not only be able to confirm the synthesis of long-lived actinides, but actually inform nuclear physics calculations of fission properties in this heavy, unstable region.

V. FISSION HOT SPOTS

With fission in the r process occurring over a large range of mass numbers, and with much of the initial fission concentrated as far out as the neutron drip line, it is not obvious how practical it is for experimental and theoretical efforts to refine our knowledge of fissioning r-process nuclei. To push experiments even a few neutron numbers out from presently-studied nuclei could require tremendous efforts. Theoretical campaigns to calculate fission yields starting from the nuclear properties assumed for a given model, such as density functional theory approaches, can assist with predictions of fission yields for nuclei far from experimental reach. However such methods can be computationally expensive. Therefore given the impracticality for experimental, and even theoretical, studies to provide information on the fission yields of all nuclei of interest to the r process, a guide as to which nuclei participate most during fission in the r process is needed. Here we provide such information by finding the "hot spots" of nuclei with the highest fission flow in our r-process calculations. To do so, we average over thirty trajectories from a 1.2–1.4 M$_\odot$ neutron star merger simulation [72] (as in Fig. 15). For each mass model considered, we report the average integrated fission flow for the neutron-induced and β-delayed fission processes which we find determine the final r-process abundances.

We confine our discussion to neutron-induced and β-delayed fission since here spontaneous fission flows are comparatively much lower. In this work we apply spontaneous fission rates determined by the phenomenological equation of Karpov et $al.$ [70] which depends on fissility (Z^2/A) and barrier height. These spontaneous fission rates are very low until $Z > 100$. Therefore, for all of the simulations considered here, r-process material tends to only encounter spontaneous fission at late times when the main abundance pattern is nearly finalized. This is consistent with previous studies which surveyed the influence of several descriptions of spontaneous fission rates [36] and observed this process to weakly influence the abundances of the second to third r-process peaks. However, given the sparsity of experimental fission data, there exist phenomenological fits to spontaneous fission half-lives which, when extrapolated into neutron-rich regions, give very high spontaneous fission rates starting at $Z > 94$ [82]. Such rates effectively cut-off the influence of neutron-induced and β-delayed fission at higher proton

numbers. Therefore, the "hotspots" reported here are meant to represent a case where neutron-induced and β-delayed fission alone shape the final r-process abundance pattern.

The averaged integrated neutron-induced and β-delayed fission flows are shown in Figs. 21 and 22. Each panel shows high fission flows are obtained in two general regions of the nuclear chart: along isotopic chains $90 < Z < 95$ where fission terminates the r-process path in A, and along the β-decay pathways of nuclei initially hung up near the $N = 184$ shell closure. The exact nuclei in each general region which will have high fission flow is strongly dependent on nuclear masses and barrier heights. The Thomas-Fermi model used in GEF as well as the FRLDM model predict a large range of nuclei with relatively low barrier heights $\sim 4 - 6$ MeV near the $N = 184$ shell closure. These models therefore show significant fission flow to the left of $N = 184$ for the neutron-rich actinide region of $89 < Z < 95$ which is where GEF yields show asymmetric yield contributions. Less of this asymmetric region is accessed by HFB-17 and ETFSI models which have higher barrier heights $\sim 6 - 8$ MeV near $N = 184$ which hinders fission of material until it moves higher in mass number during the decay back to stability.

We next identify the nuclei whose fission yields are primarily responsible for the shape of the second r-process peak. To do so we consider the threshold of integrated fission fission flow that contributes to finalizing the r-process abundance pattern. For each mass model, we apply GEF neutron-induced fission yields for the nuclei with an average integrated neutron-induced fission above a set threshold with symmetric splits assumed for all remaining nuclei. We apply the same threshold criterion for β-delayed fission. We find that applying GEF yields to only nuclei with an average integrated fission flow larger than 10^{-5} reproduces the final abundance trend almost exactly for all mass models. In the case of TF, HFB, and ETFSI models, implementing the GEF yields for only nuclei having an average integrated fission flow larger than 10^{-4} was found to be sufficient to reproduce the relative abundances.

We note Figs. 21 and 22 show many of the nuclei with fission flows higher than the 10^{-5} threshold have odd neutron number. Are these flows primarily responsible for shaping the final abundance pattern, or do even-N nuclei play a larger role? It is not immediately obvious that high odd-N flow implies a great influence on the abundance pattern since, roughly speaking, the even-N abundances are greater than those of odd-N nuclei throughout the r process. However fission, particularly in the case of neutron-induced, can have rates for an odd-N initial species which are $\sim 8 - 10$ orders of magnitude larger than their even-N isotopic neighbor. We find this disparity in the rates to dominate over the abundance preference for even-N nuclei. In fact, we find fission reactions which have an odd-N initial species to have such dominant fission flows that the r-process abundance pattern

can nearly be reproduced when GEF yields are applied to the daughters of just odd-N nuclei, as shown in Fig. 23. Therefore it is the fission rates of odd-N target nuclei and the fission yields of the corresponding even-N compound nuclei which are most impactful in r-process calculations.

To report the exact nuclei whose daughter yields are of most consequence when assuming a particular mass model, in Supplemental Materials we tabulate the nuclei that satisfy the 10^{-5} threshold criterion for each of the mass models considered. We find that all mass models predict the fission outcomes of 200 nuclei or less to be of relevance in setting the r-process abundance pattern. If only the odd-N nuclei are considered, then all mass models predict 120 nuclei or less to be of relevance. Although the nuclei which most impact the shape of the abundance pattern are dependent on the mass model and fission barriers, in Fig. 24 we highlight nuclei commonly found to have a high average integrated fission flow ($\geq 10^{-5}$) given the range of nuclear inputs considered. Note that this is essentially reporting the overlap of nuclei found to have high fission flow in Figs. 21 and 22, which was mostly determined by a given model's fission barriers. Therefore, the shape of these hotspots is highly influenced by where models agree nuclei have low $4 - 6$ MeV barrier heights. The earlier onset of neutron-induced fission, as compared to β-delayed fission, is reflected in the reach of this fission channel beyond $N = 184$ where abundances are high only at early times.

Our calculations with the nuclear inputs applied here see all four models agree upon 15 nuclei to be of importance for the neutron-induced fission channel, with over half of these found in the $Z = 93$ and 94 isotopic chains (all of which have odd-N). The β-delayed fission channel sees all models agree upon only 7 nuclei of importance, with nearly all of these nuclei in $Z = 93$ and $Z = 97$ isotopic chains and most (but not all) having odd-N. We note that since the fission yields do affect the flow of material in a fission cycling r-process, the "hotspots" found using 50/50 splits differ for a small handful of nuclei, but the overall region of importance remains the same. In previous work, the mass region with $93 \leq Z \leq 95$ and $180 \leq N \leq 186$ was identified as the dominate region for neutron-induced and β-delayed fission flow for the FRDM case considered in Ref. [15]. In Ref. [19], nuclei with $A \simeq 278$ were singled out as the isobars whose fission products determine the abundance of nuclei in the $110 \lesssim A \lesssim 170$ region. Although we also see high fission flow in this region near the $N = 184$ shell closure, we see much of the high flow concentrated at $N < 184$ since fission is still very active during the decay back to stability.

VI. CONCLUSIONS

The influence of the astrophysical conditions on whether a fission cycling r process is achieved, as well as the dependence on unknown nuclear physics proper-
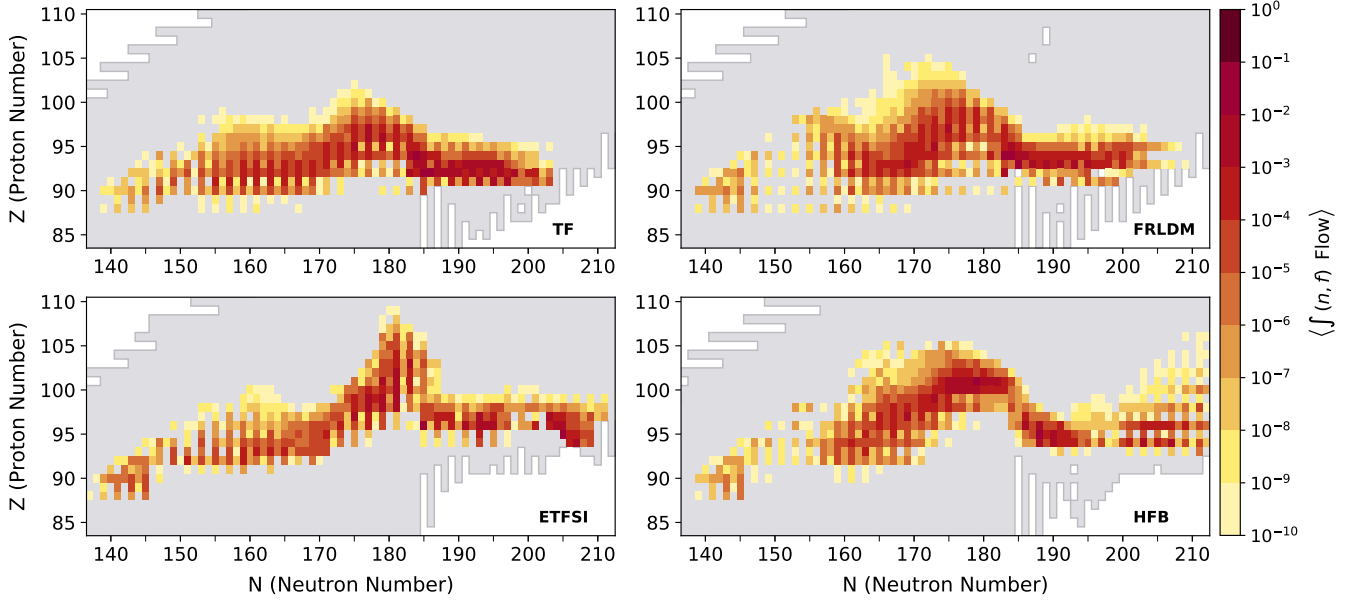
FIG. 21. (Color online) The integrated neutron-induced fission flow averaged over thirty astrophysical trajectories from a 1.2–1.4 M$_\odot$ neutron star merger simulation [72] assuming GEF (top left), FRLDM (top right), ETFSI (bottom left), and HFB-14 (bottom right) barrier heights.
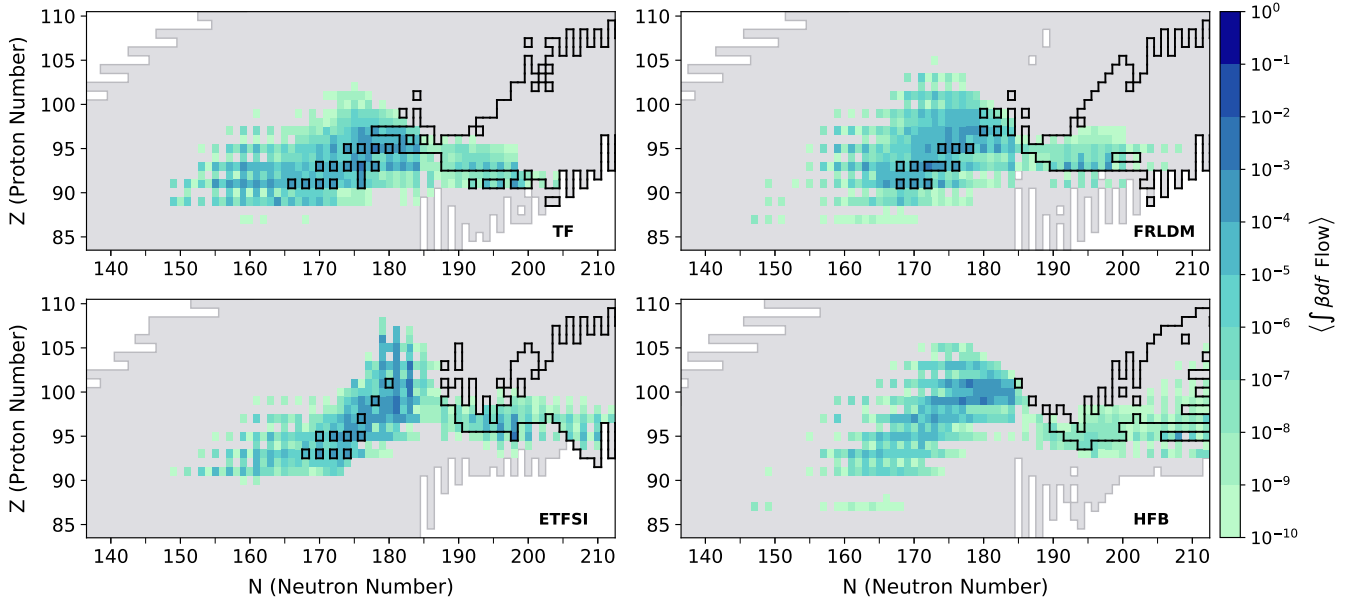

FIG. 22. (Color online) The integrated β-delayed fission flow averaged over thirty astrophysical trajectories from a 1.2–1.4 M$_\odot$ neutron star merger simulation [72] assuming GEF (top left), FRLDM (top right), ETFSI (bottom left), and HFB-14 (bottom right) barrier heights. The black outline here shows where the probability for nuclei to undergo multi-chance β-delayed fission (relative to ordinary β-decay) exceeds 10%.

ties for the heaviest neutron-rich nuclei, imply astrophysical environments which host fission to involve the greatest number of r-process uncertainties. If "red" kilonova components originate from the very neutron-rich condi-

tions seen in neutron star merger dynamical ejecta, fission most certainly plays a role in setting the lanthanide mass fraction which determines wavelength and peak luminosity. If the "red" kilonova is instead generated pri-
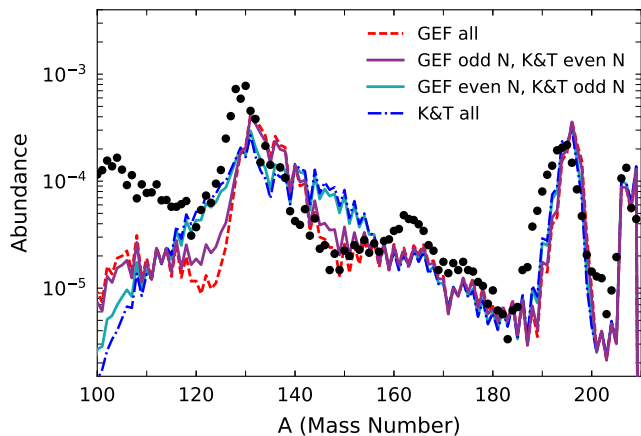
FIG. 23. (Color online) The r-process abundance pattern using the cold tidal tail conditions of trajectory 1 [72] and the FRDM2012 mass model when GEF yields are applied to all nuclei (dashed red) as compared to GEF yields for only the odd-N fission reactions of $(Z,N)(n,f)$ and $(Z,N)\beta$df (solid purple) with all other fissioning nuclei assuming the fission yields of [21] (K&T). For comparison the abundances with GEF yields applied to only the even-N fission reactions of $(Z,N)(n,f)$ and $(Z,N)\beta$df (solid blue) as well as K&T applied to all nuclei (dot-dashed dark blue) are also shown.

marily from an accretion disk wind, astrophysical uncertainties in the exact neutron richness of such conditions make it difficult to know how much the treatment of fission can influence observation. Since neutron star mergers permit many possible routes to a fission cycling r process, it is important to understand the potential impact on r-process observables from variations in the fission treatment.

We have shown that taking into account the fission yield dependence on the initial excitation energy can influence the final r-process abundances by using the publicly available GEF code to obtain sets of fission yields for neutron-induced, β-delayed, and spontaneous fission with an appropriate energy applied for each respective fission process. We considered the sensitivity of our results to the treatment of the excitation-energy sharing and de-excitation of the fission fragments using FREYA and showed that such considerations can change the average prompt neutron multiplicity by $\sim 1-3$ neutrons in the most neutron-rich regions. However, the sensitivity of the r process to the energy sharing and de-excitation treatment was found to be secondary compared to the effect of the fission yield dependence on initial excitation energy, demonstrating the treatment of the primary fragment yields to be of dominant influence in the r process. Thus careful theoretical calculations of fission fragment yields (prior to neutron emission) that are consistently derived within the framework of a given mass model are crucial to understanding lanthanide production in a fission cycling r process.

We showed that the trend in GEF yields, which transition from asymmetric to mostly symmetric yields along an isotopic chain, can reproduce the trend of the right edge of the second r-process peak seen in solar data given fission cycling conditions that reach the most neutron-rich regions beyond $N = 184$. We considered the influence of nuclear mass models by applying fission rates that self-consistently account for the dependence on nuclear masses and fission barriers. We found that the fission flow explicitly follows the regions of low $4-6$ MeV fission barrier heights making the fissioning nuclei which most impact r-process calculations model dependent. The population of key fissioning actinides, such as ^{254}Cf was also shown to sensitively depend on the fission barrier assumptions of a given model.

For each of the four sets of masses and barrier heights considered, we reported the integrated fission flow averaged over 30 simulation trajectories for a 1.2–1.4 $M_\odot$ neutron star merger to find the fissioning nuclei of most importance. The odd-even behavior observed in these fission flows lead us to identify odd-N species undergoing $(Z,N)(n,f)$ and $(Z,N)\beta$df to substantially dominate over even-N species in setting the r-process abundance pattern. The "hot spots" of key fissioning nuclei given all models considered show that nuclei of importance are often found to have $N < 184$ due to pile-up of material at this predicted shell closure. The proximity of these "hot spots" to the region of experimentally established decay data shows the potential for experiments to access some of the fissioning nuclei found to play a key role in setting the r-process abundance pattern. Efforts by experimental and theoretical nuclear physics to further the knowledge of fission properties in neutron-rich regions are necessary to develop a more complete picture of heavy element production in neutron star mergers.
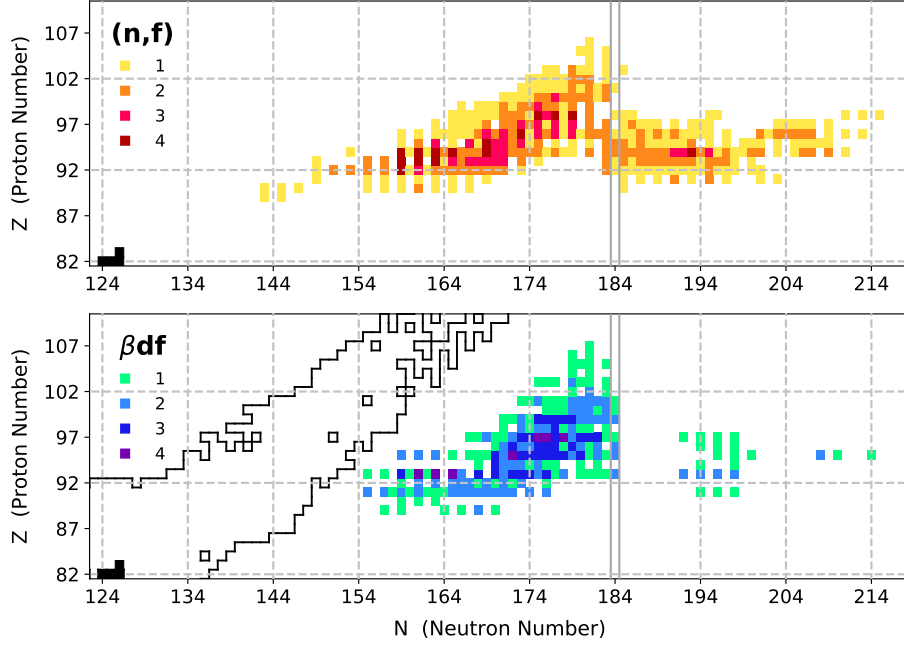
FIG. 24. (Color online) The nuclei found to have an average integrated neutron-induced (upper) /β-delayed (lower) fission flow above the 10^{-5} threshold found to control the r-process abundance pattern in one (yellow/green), two (orange/light blue), three (red/dark blue), or four (dark red/purple) of the mass models considered in Figure 21/22. The black boxes show stable nuclei while the black outline shows the location of known experimental decay rates.

Appendix A: List of Supplemental Materials

Sec. III: Integrated fission flows cross referenced with fission yields as in Fig. 7 for trajectory 17 with the TF model.

Sec. IV: Integrated fission flows cross referenced with fission yields as in Fig. 7 for trajectory 1 with the HFB model.

Sec. IV: Comparison of the r-process abundance pattern with GEF versus FREYA as in Fig. 9 for trajectory 22 with the HFB model.

Sec. IV: Integrated fission flows cross referenced with fission yields as in Fig. 7 for trajectory 1 with the FRDM model.

Sec. IV: Integrated fission flows cross referenced with fission yields as in Fig. 7 for trajectory 1 with the FRDM model and Marketin *et al.* β-decay rates.

Sec. VI: Ascii tables of nuclei with an average integrated fission flow higher than 10^{-5} for neutron-induced and β-delayed fission processes for each mass model considered. For the neutron-induced case, columns are: Z, A, flow, relative percent flow, barrier height of $(Z,A+1)$, and the neutron separation energy of $(Z,A+1)$. For the β-delayed case columns are: Z, A, flow, relative percent flow, β-delayed fission probability, barrier height of $(Z+1,A)$, β-decay Q-value of (Z,A), and the neutron separation energy of $(Z+1,A)$. When a value is marked with *, it implies that mass or fission barrier height information was unavailable for the given model, so the FRDM2012 mass value and FRLDM barrier height are instead used to determine the reaction and decay rates.

[1] G. R. Burbidge, F. Hoyle, E. M. Burbidge, R. F. Christy, and W. A. Fowler, Phys. Rev. **103**, 1145 (1956).

[2] A. P. Ji, A. Frebel, A. Chiti, and J. D. Simon, Nature **531**, 610 (2016), arXiv:1512.01558.

[3] I. U. Roederer, M. Mateo, J. I. Bailey, III, Y. Song, E. F. Bell, J. D. Crane, S. Loebman, D. L. Nidever, E. W.

Olszewski, S. A. Shectman, I. B. Thompson, M. Valluri, and M. G. Walker, AJ **151**, 82 (2016), arXiv:1601.04070 [astro-ph.SR].

[4] J. M. Lattimer and D. N. Schramm, ApJ **192**, L145 (1974).

[5] B. S. Meyer, ApJ **343**, 254 (1989).

[6] C. Freiburghaus, S. Rosswog, and F.-K. Thielemann, ApJ **525**, L121 (1999).

[7] S. Goriely, A. Bauswein, and H.-T. Janka, ApJ **738**, L32 (2011), arXiv:1107.0899 [astro-ph.SR].

[8] O. Korobkin, S. Rosswog, A. Arcones, and C. Winteler, MNRAS **426**, 1940 (2012), arXiv:1206.2379 [astro-ph.SR].

[9] S. Wanajo, Y. Sekiguchi, N. Nishimura, K. Kiuchi, K. Kyutoku, and M. Shibata, ApJ **789**, L39 (2014), arXiv:1402.7317 [astro-ph.SR].

[10] O. Just, A. Bauswein, R. A. Pulpillo, S. Goriely, and H.-T. Janka, MNRAS **448**, 541 (2015), arXiv:1406.2687 [astro-ph.SR].

[11] P. S. Cowperthwaite et al., ApJL **848**, L17 (2017).

[12] B. P. Abbott et al. (LIGO Scientific Collaboration and Virgo Collaboration), Phys. Rev. Lett. **119**, 161101 (2017).

[13] D. Kasen, B. Metzger, J. Barnes, E. Quataert, and E. Ramirez-Ruiz, Nature (London) **551**, 80 (2017), arXiv:1710.05463 [astro-ph.HE].

[14] B. Côté, C. L. Fryer, K. Belczynski, O. Korobkin, M. Chruślińska, N. Vassh, M. R. Mumpower, J. Lippuner, T. M. Sprouse, R. Surman, and R. Wollaeger, ApJ **855**, 99 (2018), arXiv:1710.05875.

[15] M. Eichler, A. Arcones, A. Kelic, O. Korobkin, K. Langanke, T. Marketin, G. Martinez-Pinedo, I. Panov, T. Rauscher, S. Rosswog, C. Winteler, N. T. Zinner, and F.-K. Thielemann, ApJ **808**, 30 (2015), arXiv:1411.0974 [astro-ph.HE].

[16] J. Barnes, D. Kasen, M.-R. Wu, and G. Martínez-Pinedo, ApJ **829**, 110 (2016), arXiv:1605.07218 [astro-ph.HE].

[17] Y. Zhu, R. T. Wollaeger, N. Vassh, R. Surman, T. M. Sprouse, M. R. Mumpower, P. Möller, G. C. McLaughlin, O. Korobkin, T. Kawano, P. J. Jaffke, E. M. Holmbeck, C. L. Fryer, W. P. Even, A. J. Couture, and J. Barnes, arXiv e-prints (2018), arXiv:1806.09724 [astro-ph.HE].

[18] S. Goriely, J.-L. Sida, J.-F. Lemaître, S. Panebianco, N. Dubray, S. Hilaire, A. Bauswein, and H.-T. Janka, Phys. Rev. Lett. **111**, 242502 (2013).

[19] S. Goriely, Eur. Phys. J. A **51**, 22 (2015).

[20] I. V. Panov, I. Y. Korneev, and F.-K. Thielemann, Astron. Lett. **34**, 189 (2008).

[21] T. Kodama and K. Takahashi, Nucl. Phys. A **239**, 489 (1975).

[22] M. Eichler, A. Arcones, R. Käppeli, O. Korobkin, M. Liebendörfer, G. Martinez-Pinedo, I. V. Panov, T. Rauscher, S. Rosswog, F.-K. Thielemann, and C. Winteler, in *Journal of Physics Conference Series*, Journal of Physics Conference Series, Vol. 665 (2016) p. 012054.

[23] S. Shibagaki, T. Kajino, G. J. Mathews, S. Chiba, S. Nishimura, and G. Lorusso, ApJ **816**, 79 (2016), arXiv:1505.02257 [astro-ph.SR].

[24] J.-J. Gaimard and K.-H. Schmidt, Nucl. Phys. A **531**, 709 (1991).

[25] A. Kelic, M. Valentina Ricciardi, and K.-H. Schmidt, arXiv e-prints (2009), arXiv:0906.4193 [nucl-th].

[26] K.-H. Schmidt, B. Jurado, C. Amouroux, and C. Schmitt, Nucl. Data Sheets **131**, 107 (2016).

[27] J. d. J. Mendoza-Temis, M.-R. Wu, K. Langanke, G. Martínez-Pinedo, A. Bauswein, and H.-T. Janka, Phys. Rev. C **92**, 055805 (2015), arXiv:1409.6135 [astro-ph.HE].

[28] J. J. Mendoza-Temis, M. R. Wu, G. Martínez-Pinedo, K. Langanke, A. Bauswein, H.-T. Janka, and A. Frank, in *Journal of Physics Conference Series*, Journal of Physics Conference Series, Vol. 730 (2016) p. 012018.

[29] I. V. Panov, I. Y. Korneev, T. Rauscher, G. Martínez-Pinedo, A. Kelić-Heil, N. T. Zinner, and F.-K. Thielemann, A&A **513**, A61 (2010), arXiv:0911.2181 [astro-ph.SR].

[30] http://www.khs-erzhausen.de/GEF-2016-1-2.html.

[31] J. M. Verbeke, J. Randrup, and R. Vogt, Comp. Phys. Comm. **191**, 178 (2015).

[32] J. M. Verbeke, J. Randrup, and R. Vogt, Comp. Phys. Comm. **222**, 263 (2018).

[33] I. Petermann, K. Langanke, G. Martínez-Pinedo, I. V. Panov, P.-G. Reinhard, and F.-K. Thielemann, Eur. Phys. J. A **48**, 122 (2012), arXiv:1207.3432 [nucl-th].

[34] S. A. Giuliani, G. Martínez-Pinedo, and L. M. Robledo, Phys. Rev. C **97**, 034323 (2018), arXiv:1704.00554 [nucl-th].

[35] F.-K. Thielemann, J. Metzinger, and H. V. Klapdor, Z. Phys. A **309**, 301 (1983).

[36] I. V. Panov, I. Y. Korneev, G. Martinez-Pinedo, and F.-K. Thielemann, Astron. Lett. **39**, 150 (2013).

[37] M. R. Mumpower, T. Kawano, T. M. Sprouse, N. Vassh, E. M. Holmbeck, R. Surman, and P. Möller, arXiv e-prints (2018), arXiv:1802.04398 [nucl-th].

[38] P. Möller, A. J. Sierk, T. Ichikawa, and H. Sagawa, At. Data Nucl. Data Tables **109**, 1 (2016), arXiv:1508.06294 [nucl-th].

[39] W. D. Myers and W. J. Swiatecki, Nucl. Phys. A **601**, 141 (1996).

[40] S. Goriely, N. Chamel, and J. M. Pearson, Phys. Rev. Lett. **102**, 152503 (2009), arXiv:0906.2607 [nucl-th].

[41] Y. Aboussir, J. M. Pearson, A. K. Dutta, and F. Tondeur, Nucl. Phys. A **549**, 155 (1992).

[42] Y. Aboussir, J. M. Pearson, A. K. Dutta, and F. Tondeur, At. Data Nucl. Data Tables **61**, 127 (1995).

[43] M.-R. Wu, J. Barnes, G. Martinez-Pinedo, and B. D. Metzger, arXiv e-prints (2018), arXiv:1808.10459 [astro-ph.HE].

[44] A. J. Koning, S. Hilaire, and M. C. Duijvestijn, in *International Conference on Nuclear Data for Science and Technology*, American Institute of Physics Conference Series, Vol. 769, edited by R. C. Haight, M. B. Chadwick, T. Kawano, and P. Talou (2005) pp. 1154–1159.

[45] A. Koning, S. Hilaire, and M. Duijvestijn, "TALYS: Nuclear Reaction Simulator," Astrophysics Source Code Library (2012), ascl:1202.004.

[46] O. Litaize, O. Serot, and L. Berge, Eur. Phys. J. A **51**, 177 (2015).

[47] P. Talou, T. Kawano, and I. Stetcu, *CGMF, Version 1.0*, Tech. Rep. (LANL Technical Report LA-CC-13-063, 2013).

[48] J. Randrup and P. Möller, Phys. Rev. Lett. **106**, 132503 (2011), arXiv:1103.0535 [nucl-th].

[49] P. Jaffke, P. Möller, P. Talou, and A. J. Sierk, Phys. Rev. C **97**, 034608 (2018), arXiv:1712.05511 [nucl-th].

[50] N. Schunck and L. M. Robledo, Rep. Prog. Phys. **79**,

116301 (2016).

[51] W. D. Myers and W. J. Swiatecki, Phys. Rev. C **60**, 014606 (1999).

[52] U. Brosa, S. Grossmann, and A. Müller, Phys. Rep. **197**, 167 (1990).

[53] S. I. Mulgin and S. V. Zhdanov, Phys. Lett. B **462**, 29 (1999).

[54] T. England and B. Rider, LANL, LA-UR, 94e3106 (1994).

[55] M. E. Gooden, C. W. Arnold, J. A. Becker, C. Bhatia, M. Bhike, E. M. Bond, T. A. Bredeweg, B. Fallin, M. M. Fowler, C. R. Howell, J. H. Kelley, Krishichayan, R. Macri, G. Rusev, C. Ryan, S. A. Sheets, M. A. Stoyer, A. P. Tonchev, W. Tornow, D. J. Vieira, and J. B. Wilhelmy, Nucl. Data Sheets Special Issue on Nuclear Reaction Data, **131**, 319 (2016).

[56] T. Rubehn, K. X. Jing, L. G. Moretto, L. Phair, K. Tso, and G. J. Wozniak, Phys. Rev. C **54**, 3062 (1996), nucl-ex/9607005.

[57] R. Vogt and J. Randrup, Phys. Rev. C **96**, 064620 (2017).

[58] J. Van Dyke, L. Bernstein, and R. Vogt, arXiv preprint arXiv:1809.05587 (2018).

[59] S. Lemaire, P. Talou, T. Kawano, M. B. Chadwick, and D. G. Madland, Phys. Rev. C **72**, 024601 (2005).

[60] R. Vogt and J. Randrup, Phys. Rev. C **90**, 064623 (2014).

[61] P. Talou, R. Vogt, J. Randrup, M. E. Rising, S. A. Pozzi, J. Verbeke, M. T. Andrews, S. D. Clarke, P. Jaffke, M. Jandel, T. Kawano, M. J. Marcath, K. Meierbachtol, L. Nakae, G. Rusev, A. Sood, I. Stetcu, and C. Walker, Eur. Phys. J. A **54**, 9 (2018), arXiv:1710.00107 [nucl-th].

[62] M. Wang, G. Audi, F. G. Kondev, W. J. Huang, S. Naimi, and X. Xu, Chin. Phys. C **41**, 030003 (2017).

[63] G. Audi, F. Kondev, M. Wang, W. Huang, and S. Naimi, Chin. Phys. C **41**, 030001 (2017).

[64] C. Sneden, J. J. Cowan, and R. Gallino, ARA&A **46**, 241 (2008).

[65] T. Kawano, M. R. Mumpower, and J. L. Ullmann, in *14th International Symposium on Nuclei in the Cosmos (NIC2016)*, edited by S. Kubono, T. Kajino, S. Nishimura, T. Isobe, S. Nagataki, T. Shima, and Y. Takeda (2017) p. 011003.

[66] M. R. Mumpower, T. Kawano, and P. Möller, in *APS Division of Nuclear Physics Meeting Abstracts* (2014) p. KD.010.

[67] M. R. Mumpower, T. Kawano, and P. Möller, Phys. Rev. C **94**, 064317 (2016), arXiv:1608.01956 [nucl-th].

[68] P. Möller, M. R. Mumpower, T. Kawano, and W. D. Myers, At. Data Nucl. Data Tables (2018), https://doi.org/10.1016/j.adt.2018.03.003.

[69] M. R. Mumpower, R. Surman, D.-L. Fang, M. Beard, P. Möller, T. Kawano, and A. Aprahamian, Phys. Rev. C **92**, 035807 (2015), arXiv:1505.07789 [nucl-th].

[70] A. V. Karpov, V. I. Zagrebaev, Y. Martinez Palenzuela, L. Felipe Ruiz, and W. Greiner, Int. J. Mod. Phys. E **21**, 1250013-1-1250013-20 (2012).

[71] V. I. Zagrebaev, A. V. Karpov, I. N. Mishustin, and W. Greiner, Phys. Rev. C **84**, 044617 (2011).

[72] S. Rosswog, T. Piran, and E. Nakar, Mon.Not. R. Astron. Soc. **430**, 2585 (2013), arXiv:1204.6240 [astro-ph.HE].

[73] T. Piran, E. Nakar, and S. Rosswog, Mon.Not. R. Astron. Soc. **430**, 2121 (2013), arXiv:1204.6242 [astro-ph.HE].

[74] O. Korobkin, S. Rosswog, A. Arcones, and C. Winteler, Mon.Not. R. Astron. Soc. **426**, 1940 (2012), arXiv:1206.2379 [astro-ph.SR].

[75] A. W. Steiner, M. Hempel, and T. Fischer, ApJ **774**, 17 (2013), arXiv:1207.2184 [astro-ph.SR].

[76] P. Möller, A. J. Sierk, T. Ichikawa, A. Iwamoto, R. Bengtsson, H. Uhrenholt, and S. Åberg, Phys. Rev. C **79**, 064304 (2009).

[77] P. Möller, A. J. Sierk, T. Ichikawa, A. Iwamoto, and M. R. Mumpower, Phys. Rev. C **91**, 024310 (2015).

[78] A. Mamdouh, J. M. Pearson, M. Rayet, and F. Tondeur, Nucl. Phys. A **644**, 389 (1998).

[79] A. Mamdouh, J. M. Pearson, M. Rayet, and F. Tondeur, Nucl. Phys. A **679**, 337 (2001), nucl-th/0010093.

[80] S. Goriely, in *Tours Symposium on Nuclear Physics V*, American Institute of Physics Conference Series, Vol. 704, edited by M. Arnould, M. Lewitowicz, G. Münzenberg, H. Akimune, M. Ohta, H. Utsunomiya, T. Wada, and T. Yamagata (2004) pp. 375–384.

[81] T. Marketin, L. Huther, and G. Martínez-Pinedo, Phys. Rev. C **93**, 025805 (2016), arXiv:1507.07442 [nucl-th].

[82] C. Xu and Z. Ren, Phys. Rev. C **71**, 014309 (2005).